



Provided by the author(s) and University of Galway in accordance with publisher policies. Please cite the published version when available.

Title	An experimental and kinetic modeling study of n-hexane oxidation
Author(s)	Zhang, Kuiwen; Banyon, Colin; Togbé, Casimir; Dagaut, Philippe; Bugler, John; Curran, Henry J.
Publication Date	2015-09-11
Publication Information	Zhang, KW, Banyon, C, Togbe, C, Dagaut, P, Bugler, J, Curran, HJ (2015) 'An experimental and kinetic modeling study of n-hexane oxidation'. Combustion And Flame, 162 :4194-4207.
Publisher	Elsevier
Link to publisher's version	<a href="http://www.sciencedirect.com/science/article/pii/S0010218015002576">http://www.sciencedirect.com/science/article/pii/S0010218015002576</a>
Item record	<a href="http://hdl.handle.net/10379/5639">http://hdl.handle.net/10379/5639</a>
DOI	<a href="http://dx.doi.org/10.1016/j.combustflame.2015.08.001">http://dx.doi.org/10.1016/j.combustflame.2015.08.001</a>

Downloaded 2024-05-18T18:04:25Z

Some rights reserved. For more information, please see the item record link above.



# An experimental and kinetic modeling study of *n*-hexane oxidation

Kuiwen Zhang<sup>1</sup>, Colin Banyon<sup>1</sup>, Casimir Togbé<sup>2</sup>, Philippe Dagaut<sup>2</sup>, John Bugler<sup>1</sup>, Henry J. Curran<sup>1\*</sup>

<sup>1</sup>*School of Chemistry, National University of Ireland Galway, Ireland*

<sup>2</sup>*CNRS-INSIS, 1C avenue de la recherche scientifique, 45071 Orléans cedex 2, France*

## Abstract

Ignition delay times for *n*-hexane oxidation have been measured in a rapid compression machine (RCM) at stoichiometric conditions at 15 bar. Due to the high reactivity of *n*-hexane and non-ideal experimental effects associated with measuring short ignition delay times in the RCM (i.e. under 5 ms), further experiments were performed in a high-pressure shock tube for multiple fuel mixtures at equivalence ratios of  $\phi = 1$  and  $\phi = 2$  over the temperature range of 627–1365 K at pressures of 15 and 32 bar. To further study the concentration of intermediate species during the oxidation process, experiments have also been carried out in a jet-stirred reactor over a wide temperature range of 530–1160 K at 10 atm pressure and at equivalence ratios of  $\phi = 0.5$ , 1.0 and 2.0. Species which include reactants, intermediates and products were identified and quantified as a function of temperature. These experimental results were used to aid the development and validation of a detailed kinetic model. The low-temperature chemistry of *n*-hexane has been refined by adopting alternative isomerization reactions for peroxy hydroperoxy-alkyl ( $\dot{\text{O}}_2\text{QOOH}$ ) radicals, leading to more detailed chemistry for this type of intermediate with multiple product channels. This mechanism has adopted a series of new reaction rates and rate rules mostly from recently reported high-level calculations. Slight modifications have been made to the suggested reaction rates and rate rules within their reported uncertainty ranges to achieve better agreement with the experimental results for both ignition delay times and speciation measurements. The new model has been validated against the experimental data presented here, with an overall good agreement compared to the experimental results. The molecular structure of *n*-hexane is more representative of normal alkanes that may be found in transportation relevant fuels (e.g. gasoline) compared to those with shorter carbon chains which is important in developing a robust sub-mechanism of base chemistry for larger, more practical fuels. Since the modified reaction rate rules presented in this work have shown to successfully predict the oxidation kinetics of *n*-hexane, these rate rules could be the basis for the development of mechanisms for even larger normal alkanes that are more representative of diesel and jet fuels. As a further demonstration of the utility of the rate rules the revised rules are shown to well predict the ignition delay times and the low temperature species concentrations of *n*-heptane from previous studies.

## Introduction

Chemical kinetic mechanisms describing the oxidation of alkane molecules are receiving increased attention within the combustion community due to the large amount of this type of species found in transportation fuels and their surrogates. These predictive models are invaluable toward the design of future combustion technologies that can achieve high fuel efficiencies while emitting low levels of toxic and climate altering pollutants [1–3]. The development of accurate low-temperature oxidation mechanisms is especially important for assigning ignition timing and rate-of-heat-release in kinetically controlled, low-temperature combustion strategies such as HCCI, RCCI and PPC, which all hold promise for clean, efficient transportation engines [4]. The oxidation mechanisms of small alkanes, from methane to butane, have been studied over a wide range of conditions both experimentally and theoretically [5–13]. An abundance of work has been performed on characterizing the oxidation chemistry of these small fuels because of the practical importance of these species as constituents in natural gas, while also providing the building blocks for mechanisms focused on larger hydrocarbons [14–15]. Much attention has also been focused on larger alkanes such as *n*-heptane and *iso*-octane due to their relevance to liquid fuels used in practical combustors, where they serve as primary reference fuels [16–22].

In comparison, intermediate length alkanes such as the hexanes have been less studied [23–27]. Previous work has focused mainly on the high-temperature oxidation of hexane, however few studies have been conducted at low-temperature conditions [25, 27–28]. In 1996, Burcat *et al.* measured ignition delay times for *n*-hexane-oxygen-argon mixtures in a shock tube over the temperature range of 1020–1725 K at pressures of 1–7 atm [23]. A mechanism with 386 elementary reactions was validated against the experimental results. In 2004, Zhukov *et al.* reported ignition delay times for *n*-hexane at much higher pressures of 60–220 atm, in the temperature range of 1000–1100 K [26]. The kinetic model published by Curran *et al.* for *n*-heptane was used by Zhukov *et al.* to simulate the reported shock tube data with satisfactory agreement [17]. However, these studies focused on the high temperature conditions and neglected to validate the *n*-hexane mechanism in the low-temperature regime.

In 2014, Mével *et al.* studied the oxidation of *n*-hexane in a flow reactor at low temperatures [25] where *n*-hexane was used as a single component surrogate for kerosene. The temperature range investigated was 450–1000 K at a pressure of 1 bar. The gas phase mixture composition was measured by both laser-based diagnostics and gas chromatography at the outlet of the reactor. The species measured by these techniques were limited to reactants, C<sub>2</sub>–C<sub>5</sub> olefins and major products such as H<sub>2</sub>O, CO and CO<sub>2</sub>. The model of Ramirez *et al.* [29] has reproduced most of the reported experimental trends. However, the detection of more species such as alkyl peroxides and cyclic ethers is needed to provide a better insight into the important low-temperature chemistry pathways.

A recent study was reported by Wang *et al.* [27] where the low-temperature oxidation of the five isomers of hexane were investigated in a jet-stirred reactor (JSR) between 550–1000 K at 1 atm. Intermediate species concentrations were measured by both gas chromatography-mass spectrometry (GC-MS) and synchrotron vacuum ultraviolet photoionization mass spectrometry (SVUV-PIMS) techniques [30], where species concentration measurements obtained from both methods were in good agreement. Cyclic ethers, which are important intermediates formed in the negative temperature coefficient (NTC) region [31], were identified and quantified for all five isomers, providing valuable data for the validation of kinetic models in the NTC region.

The current study reports newly acquired experimental data for *n*-hexane and a newly developed kinetic model for *n*-hexane oxidation. Ignition delay times of stoichiometric *n*-hexane mixtures in synthetic air (i.e. 21% O<sub>2</sub> and 79% diluent) have been measured both in a rapid compression machine (RCM) and high-pressure shock tube between temperatures of 627–1365 K at a pressure of 15 and 32 bar. To further investigate reactant, intermediate and final species formation, experiments were conducted in a JSR in the temperature range of 530–1160 K at 10 atm. Species were identified and their concentration were measured as a function of temperature. These data have been used to validate the updated detailed chemical kinetic oxidation mechanism which is also presented here. The current work is an extension of our previous works on *n*-alkanes, which is a continuous effort to develop the oxidation mechanisms of alkanes in a hierarchical manner. New reaction pathways are adopted in the updated mechanism particularly in the low-temperature region that include alternative isomerization reactions for hydroperoxyl alkyl peroxides, which produce di-hydroperoxyl alkyl radicals that in turn have multiple decomposition channels by analogy to that of hydroperoxyl alkyl radicals. Reaction rates in the updated mechanism are determined from analogy to the rate rules which were previously utilized for *n*-pentane, but have been slightly modified within the rate constant uncertainty range in order to obtain better agreement with the experimental data. The details of the impact of the modifications in reaction rate rules on *n*-hexane will be presented and discussed.

## **Experimental Methods**

### *Rapid compression machine*

Low-temperature (600–750 K) ignition delay times were measured in the NUIG rapid compression machine. This is a clone of the RCM originally built by Affleck and Thomas [32], and re-commissioned at NUI Galway by Brett *et al.* [33]. Briefly, two opposed pistons volumetrically compress a fuel mixture in about 16 ms to create and maintain a high temperature and pressure environment. At the end of the stroke the pistons are locked, allowing a constant volume reaction to proceed. The pistons are pneumatically driven and locked, while a chamber filled with hydraulic oil along the connecting rod is

used to actuate the pistons and control their trajectory. The machine has a 168 mm stroke and 38.2 mm bore. The fuel mixture pressure-time history is recorded in the reaction chamber using a Kistler 601A pressure transducer mounted in the sidewall of the machine. Piston positioning is monitored using a Positek P100 linear inductive position sensor, which is inserted into the machine's hollow connecting rod. The pressure transducer signal is amplified by a Kistler 5018 charge amplifier unit. Both the pressure and piston position signals are recorded by a PicoScope 4424 digital oscilloscope at 50 MHz with 8-bit resolution. The oversampled reaction chamber pressure signal is then smoothed during post-processing by employing a digital low-pass filter with a cut-off frequency of 2.7 kHz. Ignition delay times are measured from the reaction chamber pressure-time histories, which are taken as the time between the end of compression and the maximum rate of pressure rise due to the main chemical heat release, as illustrated in Fig. 2. A steep pressure rise was observed for all of the ignition events investigated here.

Compressed gas temperatures were varied by adjusting the initial temperature of the reaction chamber surfaces via an electrical heating system around the reaction chamber. Great care has been taken to reduce thermal stratification within the reaction chamber, and details of this system are available elsewhere [34]. The reaction chamber is heated to a maximum temperature of 120 °C to avoid the degradation of mechanical seals within the machine. For this study, experiments were conducted in a 0.65 CO<sub>2</sub>:0.35 N<sub>2</sub> diluent to allow access to the low temperature regime. The compressed pressure was held at 15 bar to within 1% for all of the experiments presented here by adjusting the initial fuel mixture fill pressure.

The RCM employs creviced piston heads, as illustrated in Fig. 1, which have been shown through several experimental and computational studies to suppress the formation of in-cylinder roll-up vortices within the boundary layer gases. The suppression of these vortices significantly reduces in-cylinder inhomogeneities. The current geometry of the pistons are a modified design of the optimum that is suggested by Würmel *et al.* [35], which is shown in Fig. 1. These were designed with a large crevice volume to extend the RCM to low pressure, and high-argon concentration conditions.

While the geometrically optimized creviced pistons minimize advective heat transfer from the cool boundary layer gases into the fuel charge, enthalpic losses from the test gases to the piston crevice volumes as well as diffusive heat flux from the hot charge to the cool reaction chamber walls must be accounted for to make suitable comparisons between experimental RCM data and chemical kinetic models. This is achieved here by employing a two-zone model for the in-cylinder gases, where one zone contains the small volume of inhomogeneous, non-reactive boundary layer gases while the other contains the homogenous, reactive 'adiabatic core' gases. Mechanical equilibrium is assumed between the two zones, and the homogenous reactor model (HRM) temperature is obtained by isentropically compressing or expanding the 'adiabatic core' volume at a rate derived from the experimentally measured pressure

history. However, to isolate the effects of transport processes from chemical heat release in the measured pressure histories it is necessary to compress a non-reactive mixture at each experimental condition with matched transport properties of the reactive mixture; an example is shown in Fig. 2. In this study, ‘adiabatic core’ expansion rates are determined at each experimental condition by compressing an additional fuel mixture, where the oxygen fraction is replaced with nitrogen.

The test fuel *n*-hexane (96%) was supplied by TCI UK, and used without further purification. The impurity is most likely 3-methyl pentane, which has been identified as the main impurity in the *n*-hexane used in the jet-stirred reactor experiments. The effect of this impurity on the simulated ignition delay times is minor, which has been shown in Fig. S1 in the Supplemental Material. Nitrogen (99.95%), oxygen (99.5%) and carbon dioxide (99.5%) gases were supplied by BOC Ireland. Fuel, oxygen and diluent mixtures were prepared in an external stainless steel mixing vessel. Mixtures were prepared by partial pressure, where the liquid fuel was injected and the tank heated to promote vaporization. Test mixtures were allowed to diffusively mix for 12 hours before experiments were conducted.

### *Shock tube*

Intermediate- and high-temperature (750–1300 K) ignition delay times for mixtures of *n*-hexane in air were measured in the NUIG high-pressure shock tube (HPST), described previously [36]. Briefly, the 63.5 mm bore tube is comprised of a 3 m driver section and a 5.73 m driven section, which are separated by a 3 cm diaphragm section. A double-diaphragm bursting mechanism that utilizes pre-scored, aluminium diaphragms is employed to reach high-pressure reflected shock conditions. Typically, a thin downstream diaphragm is used to promote an ideal bursting and minimize undesirable fluid dynamics during shock formation. The shock velocity is interpolated at five locations along the driven section to account for shock attenuation by measuring the incident shock arrival times at six axially staggered, sidewall mounted PCB 113B24 pressure transducers. The endwall shock velocity is calculated by linearly extrapolating the five velocities to the endwall. Pressure-time histories at the shock tube endwall are monitored using a Kistler 603B pressure transducer mounted flush with the endwall. All pressure signals are recorded using two Handyscope HS4-50 digital oscilloscopes sampling each signal at 5 MHz with 12-bit resolution. Ignition delay times are measured via the endwall pressure transducer, and are taken to be the time difference between the arrival of the shock wave at the endwall and the arrival of the Von Neumann spike due to ignition, as illustrated in Fig. 3. Well-defined ignition events have been observed for all of the conditions investigated here.

Test gas temperatures and pressures behind the reflected shock were varied by altering the shock velocity, which was achieved in two ways. For experiments that resulted in short ignition times (i.e. less than 1 ms), the total pressure of pure helium driver gas was varied. For experiments that resulted in long

ignition times (i.e. greater than 1 ms), the helium driver gas was doped with 0–20% nitrogen where the total driver gas pressure and nitrogen fraction were simultaneously varied to achieve a tailored interface at the desired reflected shock conditions. For each condition in this study the pressure behind the reflected shock wave was held constant at either 15 or 30 bar to within 10% by adjusting the initial test gas pressures.

The test gas temperature and pressure behind the reflected shock wave are calculated from the endwall shock velocity by solving the 1-D Euler equations with Rankine-Hugoniot jump conditions across the shock. The species thermochemistry used is consistent with that used to develop the kinetic model. Interactions between the shock wave and the boundary layer gases, which lead to a characteristic constant rate of pressure rise (i.e.  $dp/dt = 3\%$  per ms), were small for the conditions investigated here. Since, for this study, nearly constant temperature and pressure conditions are maintained behind the reflected shock, adequate comparisons of experimental results and kinetic mechanisms are achieved by simulating constant volume HRMs at the reflected shock conditions.

Mixtures were prepared in the same manner as described for the RCM, but the mixing vessels were fitted with a stirring mechanism. The driven section of the shock tube was also heated to prevent fuel condensation prior to an experiment. Mixtures were allowed to homogenize for 20 minutes with active stirring before experiments were conducted. For the RCM and HPST experiments presented here the estimated uncertainties are  $\pm 15\%$  for ignition delay time and  $\pm 2\%$  for temperature.

#### *Jet-stirred reactor*

Measurements of stable intermediate species concentrations were conducted in the jet-stirred reactor (JSR) at CNRS, Orleans. A detailed description of the experimental setup of the JSR is available in previous publications [37, 38]. The fuel (95% purity with 5% impurity of 3-methyl pentane) is delivered using an HPLC pump (Shimadzu LC10-AD-VP) fitted with an online degasser (DGU-20-A3) to an atomizer-vaporizer at a temperature of about 500 K. Nitrogen was used for fuel dilution to prevent possible pyrolysis and minimize the heat release in the reactor. High purity oxygen was used as the oxidizer (99.995% pure, Air Liquide). The gas phase reactants travelled through four nozzles opposed in pair with inner diameters of 1mm to produce stirring and mix the reactants in the reactor, which is a silica sphere with 4 cm diameter. A thermocouple with 0.1 mm diameter (Pt-Pt/Rh-10% in a thin-wall silica tube) was used to measure the temperature in the reactor along the vertical axis, indicating good thermal homogeneity had been achieved, that is, within 3 K/cm.

The pressure in the reactor was kept at 10 atm. The residence time remained 0.7 second and the temperature was varied step wise over the temperature range of 530 ~ 1160 K. The residence time is calculated as

$$t = \frac{V}{F} \times \frac{P_1}{P_2} \times \frac{T_2}{T_1}$$

Here  $V$  is the volume of the reactor ( $\text{cm}^3$ ),  $F$  is the total gas flow rate ( $\text{cm}^3/\text{s}$ ),  $P_1$  and  $T_1$  are the pressure and the temperature in the reactor,  $P_2$  and  $T_2$  are the ambient pressure and room temperature.

The gas phase mixture in the reactor was sampled through a low pressure sonic probe and transferred through a Teflon line heated to  $200\text{ }^\circ\text{C}$ . A Fourier transform infrared spectroscopy (20 kPa) was used to analyze the sampled gases online. Off-line analyses were performed for the samples stored in 1L Pyrex bulbs (ca. 4–6 kPa). While Fourier transform infrared (FTIR) spectroscopy was used to quantify  $\text{H}_2\text{O}$ ,  $\text{CO}$ ,  $\text{CO}_2$ ,  $\text{CH}_2\text{O}$ ; all of the other species were measured by gas chromatography ( $\text{O}_2$  and  $\text{N}_2$  by a thermal conductivity detector while a flame ionization detector was used for measuring the others species.) The experimental results have shown good repeatability and carbon balance (ca.  $100 \pm 20\%$ ) The experiment had been performed under three different equivalence ratios of 0.5, 1.0 and 2.0. The detailed composition of the inlet gas mixture for each equivalence ratio is shown in Table 1. For the JSR experiments the uncertainties in reactor temperature ( $\pm 3\text{K}$ ), residence time ( $\pm 0.05\text{s}$ ) and reactor pressure ( $10 \pm 0.1\text{ atm}$ ) are given in the experimental section. Inlet concentration uncertainties are less than  $\pm 5\%$  for reactants; for measured species an uncertainty of  $< \pm 10\%$  was determined for concentrations higher than 10 ppm.

### Chemical Kinetic Mechanism

The *n*-hexane mechanism in this work, which includes 919 species and 3952 reactions, uses AramcoMech1.3 as a sub-mechanism [13]. AramcoMech1.3 describes the oxidation of  $\text{C}_1$ - $\text{C}_2$  hydrocarbon and oxygenated fuels including: methane, ethane, ethylene, propene, acetylene, formaldehyde, acetaldehyde, methanol, ethanol and di-methyl ether. This mechanism has been validated against a variety of experimental results across a wide range of conditions [13]. Most recently, the sub-mechanism for the three pentane isomers has been updated [39]. The *n*-hexane sub-mechanism has been built based on previous mechanisms [17, 40] with the addition of several new reaction pathways. Figure 4 shows a reaction path diagram for the oxidation of alkanes, where this general framework has been adopted in the previous studies as well as the current study. The grey arrows represent reaction classes that have been included in previous alkane mechanisms as well as the current *n*-hexane mechanism [40], while open arrows are used to indicate newly added reaction classes to the current mechanism, which will be described in detail below. Several representative species relevant to the oxidation of *n*-hexane are shown in Table 2. A mechanism for 3-methyl pentane has also been developed since it was identified as an impurity in the commercially available fuel used in the JSR experiments presented here, which



accounts for 5% of the fuel mole fraction in the JSR experiment. Similar reaction pathways and rate rules have been adopted for the 3-methyl pentane sub-mechanism and *n*-hexane mechanism. However, the details regarding the development and performance of the 3-methyl pentane mechanism will not be discussed here. The kinetic model used in this work is available in the Supplemental Material.

### *High temperature mechanism*

The high-temperature mechanism for *n*-hexane developed here is based on the *n*-hexane portion of the *n*-heptane mechanism proposed by Curran *et al.* [17]. The high temperature oxidation regime is relatively simple compared to the low-temperature regime. This can be observed from inspection of the lower part of Fig. 4.

The pressure-dependent rate constants for the uni-molecular decomposition of *n*-hexane were calculated based on the estimated high-pressure limit rate constants for radical recombination reactions, using Quantum-Rice-Ramsperger-Kassel/Modified Strong Collision (QRRK/MS) theory and the CHEMRev software package [41]. The computationally efficient QRRK/MS method is employed here since good agreement has previously been obtained between this method and the more precise Rice-Ramsperger-Kassel-Marcus/Master Equation (RRKM/ME) approach for alkane decomposition [42]. The Lennard-Jones parameters for *n*-hexane have been reported by Jasper and Miller [43], which are  $\sigma = 4.37$  Å and  $\epsilon = 201$  cm<sup>-1</sup> in a bath gas of N<sub>2</sub>. The branching ratio of hydrogen abstraction from different sites of the fuel by the radical pool has a significant effect within both the low- and high-temperature regimes since this branching ratio determines the ratio of formation of the different fuel-derived radicals. Therefore, the product distributions of the following beta-scission reactions of alkyl radicals at high temperatures or alkyl radical addition to molecular oxygen at low temperatures are also affected by the hydrogen abstraction branching ratio.

Hydrogen-atom abstraction by  $\dot{\text{O}}\text{H}$  radicals is the most important H-atom abstraction reaction for hydrocarbon oxidation. Recently, Sivaramakrishnan and Michael proposed rate rules for hydrogen abstraction by  $\dot{\text{O}}\text{H}$  radicals from saturated alkanes [44], including abstraction of various types of primary, secondary, and tertiary H-atoms, which have been adopted in our mechanism. The rate constants of hydrogen-atom abstraction by  $\text{H}\dot{\text{O}}_2$  radicals are from [17].

Tsang *et al.* derived the high-pressure limit rate constants for the decomposition of *n*-hexyl radicals from experiments that were performed in a single pulse shock tube over a temperature range of 890–1020 K at pressures of 1.5–5.0 bar [45]. The rate constants of the isomerization reactions of *n*-hexyl radicals were also obtained by combining these experimental results with other literature values of the beta bond scission reactions of hexyl radicals. Tsang *et al.* suggested that the fall-off effect may become insignificant as the size of the molecule increases, while the isomerization process becomes more

important with increasing chain length. Therefore the high-pressure limit rate constants for the decomposition and isomerization of  $n$ -hexyl radicals are used directly in the mechanism without further consideration of pressure effects, as fall-off from the high-pressure limit is negligible for  $n$ -hexane at the conditions investigated here. Figure S2 in the Supplemental Material compares the simulations using high pressure limit rate constants [45] and pressure dependent rate coefficients calculated using Quantum-Rice-Ramsperger-Kassel/Modified Strong Collision (QRRK/MSK) theory. Almost no difference has been observed in the predicted ignition delay times.

### *Low temperature mechanism*

At low-temperatures fuel consumption is initiated by H-atom abstraction from the fuel, which produces alkyl radicals ( $\dot{R}$ ). These alkyl radicals can add to molecular oxygen to form alkylperoxy radicals ( $R\dot{O}_2$ ), which in turn isomerize into hydroperoxyl-alkyl radicals ( $\dot{Q}OOH$ ). Thereafter, these  $\dot{Q}OOH$  radicals can again add to molecular oxygen (i.e. the second addition to  $O_2$ ) to produce hydroperoxyl alkylperoxy radicals ( $\dot{O}_2QOOH$ ). The reaction pathways for this process are illustrated in the upper part of Fig.4. This is a chain propagating process. It was previously assumed [17, 40] that the only consumption channel for  $\dot{O}_2QOOH$  is a single step reaction where the internal transfer of a hydrogen atom to form a di-hydroperoxyl radical and the subsequent decomposition of this radical into keto-hydroperoxides occurs simultaneously. The formation and decomposition of keto-hydroperoxides is a chain branching process because it produces three radicals (two  $\dot{O}H$  radicals and one alkoxy radical). However, this is based on the assumption that the C–H bonds on the carbon atom neighboring the hydroperoxyl group are much weaker than analogous C–H bonds on a regular alkyl chain. While this assumption is reasonable, a more precise approach is warranted to adequately describe the complexities of low-temperature oxidation chemistry.

In this work, the single step approximation for the decomposition of  $\dot{O}_2QOOH$  radicals to ketohydroperoxides has been relaxed, where new reaction pathways for the consumption of  $\dot{O}_2QOOH$  radicals have been considered as illustrated in Fig. 4 by open arrows.  $\dot{O}_2QOOH$  radicals are now allowed to undergo internal H-atom transfer from carbons other than the carbon atom that neighbors the hydroperoxyl group, forming a di-hydroperoxyl alkyl radical ( $\dot{P}(OOH)_2$ ). This kind of intermediate contains two hydroperoxyl groups attached to two different carbon atoms and one radical site on a third carbon atom, which is similar to a  $\dot{Q}OOH$  radical in structure but with an additional hydroperoxyl group. The inclusion of alternative isomerization pathways is especially important for branched alkanes which contain at least one tertiary carbon atom. With the previous assumption, a  $\dot{O}_2QOOH$  radical with the hydroperoxyl group on a tertiary carbon could not isomerize via internal hydrogen abstraction because there is no hydrogen atom on this tertiary carbon. Thus further chain propagation is inhibited and the

overall reactivity would be artificially decreased. However,  $\dot{P}(\text{OOH})_2$  radicals can now be produced in the current mechanism via the alternative isomerization reactions. Depending on the locations of the hydroperoxyl groups and radical sites, the decomposition of  $\dot{P}(\text{OOH})_2$  radicals can still contribute to chain branching via beta-scission reactions during which the O–O bonds break to produce two  $\dot{\text{O}}\text{H}$  radicals. Another pathway considered is the formation of hydroperoxyl cyclic ethers, which decompose easily due to the relatively weak O–O bond in the hydroperoxyl moiety. Therefore, the formation of hydroperoxyl cyclic ethers is also a chain branching reaction with two  $\dot{\text{O}}\text{H}$  radicals produced in total. At intermediate temperatures, the concerted elimination of  $\text{H}\dot{\text{O}}_2$  radicals from  $\text{R}\dot{\text{O}}_2$  radicals becomes competitive with the isomerization of  $\text{R}\dot{\text{O}}_2$  radicals to produce  $\dot{\text{Q}}\text{OOH}$  radicals, as does its dissociation reaction back to  $\dot{\text{R}} + \text{O}_2$ . The concerted elimination reactions of  $\text{H}\dot{\text{O}}_2$  radicals have also been considered for  $\dot{\text{O}}_2\text{QOOH}$  radicals by analogy with those for  $\text{R}\dot{\text{O}}_2$  species. These reactions could be considered as a chain propagating step since only one  $\dot{\text{O}}\text{H}$  radical is produced from the formation and decomposition of olefinic hydroperoxides.

A series of quantum chemical calculations have been reported on the low-temperature oxidation reactions of alkanes [46–50]. However, few of these calculations have been performed for *n*-hexane or larger fuels. Reaction rate rules have been proposed in these studies, which are commonly statistically averaged reaction rates for generalized reaction classes that occur in specific structures for a variety of molecules, with less consideration of the influence of the neighboring molecular structures. Thus, these rules have to be used with caution considering the uncertainties induced from quantum chemical calculations and statistical methods used to generate the rate rules, as well as an inadequate comparison for target molecular structures which are too specific to be adequately captured by a generalized rate rule. Due to these uncertainties in the suggested rate rules and the difficulty of performing high level *ab-initio* calculations for all of the relevant reactions, modifications to the suggested rate rules within the reported uncertainty range have been made in some instances to achieve better agreement between the mechanism and the experimental results both in reactivity and speciation. The details of these modifications are listed in Table 3. Since over one hundred reactions are relevant to these modifications, their detailed rate constants will not be listed here, however these are available from the model in the Supplemental Material. For *n*-pentane and smaller alkanes, these modifications have not been applied since many specific rate constants from *ab-initio* calculations are available for these alkanes.

The rate rules from Miyoshi [51] are used for the addition of alkyl radicals to molecular oxygen, which are based on calculations using variational transition state theory (VTST) and RRKM/ME calculations. Rate constants for the  $\dot{\text{Q}}\text{OOH}$  radical addition to  $\text{O}_2$  (second addition to  $\text{O}_2$ ) has been calculated for the propyl +  $\text{O}_2$  system by Goldsmith *et al.* [46], however using these rate constants as a direct analogy for the hydroperoxyl hexyl +  $\text{O}_2$  system may not be accurate since the length of the carbon chain of the propyl and hexyl is significantly different. Therefore, for the second addition to  $\text{O}_2$  we use

rate constants for the first addition to  $O_2$  proposed by Miyoshi [51] with the A-factor decreased by a factor of 2, which is the same trend as with the propyl +  $O_2$  system reported by Goldsmith *et al.* [46]. To the best of our knowledge, the calculation on the propyl system by Goldsmith is the only reported investigation of  $\dot{Q}OOH + O_2$  rates. In other n-heptane mechanisms estimated, identical rate constants for both  $\dot{Q}OOH + O_2$  and  $R + O_2$  are used, for example LLNL [17] and POLIMI [52]. The rate rules employed by the current mechanism for these important reactions are expected to be more accurate than previous mechanisms due to their *ab-initio* origins compared with previously made estimates.

Villano *et al.* [49] developed the reaction rate rules for the formation of cyclic ethers and the beta-scission reactions of  $\dot{Q}OOH$  radicals as linear functions of the heat of reaction. Villano *et al.* also reported that the uncertainty in the A-factors is a factor of two, while the uncertainty in the activation energy is  $\pm 1$  kcal mol<sup>-1</sup>. These rate rules are adopted in the n-hexane mechanism but modifications have been made to the rate constants within their expected uncertainty (detailed in Table 3, row 2) to obtain better agreement with the ratios of measured concentrations of cyclic ethers in the JSR.

The reaction rates for the concerted elimination of  $\dot{R}O_2$  radicals has been calculated by Villano *et al.* in both the forward and reverse directions [48, 50]. However, at lower temperatures the forward rate constants derived through microscopic reversibility [50] utilizing the CHEMRev software package [41] are inconsistent with previous results [48], which are caused by both errors in the thermodynamic data estimated by THERM [53] and in the quantum chemical calculations [48, 50]. In addition, the rate rules from [48] and [50] were derived from a series of calculated rate constants, which were not identical to the calculated results for each reaction and contribute to the inconsistency. Therefore, the reaction rate constants for the concerted  $\dot{H}O_2$  elimination are adopted by analogy to the calculated results for n-pentane [48], with modifications (Table 3, row 3) within the uncertainty range to obtain better agreement with the experimental results.

Meanwhile, the rate rules for the beta-scission of the C–O bond in beta-hydroperoxyl alkyl radicals producing an olefin and an  $\dot{H}O_2$  radical as well as the decomposition of the  $\dot{Q}OOH$  radicals via beta-scissions, have been adopted from the calculations of Villano *et al.* [49].

Due to the similarity between  $\dot{Q}OOH$  and  $\dot{P}(OOH)_2$  radicals, the analogy and rate rules have been applied to  $\dot{P}(OOH)_2$  radicals by analogy with reactions of  $\dot{Q}OOH$  radicals, including the formation of hydroperoxyl cyclic ethers, concerted  $\dot{H}O_2$  elimination reactions and C–O bond beta-scissions producing olefinic hydroperoxides, as well as decomposition via beta-scission reactions. Since the same rate rules have been used for reactions involving  $\dot{Q}OOH$  and  $\dot{P}(OOH)_2$  radicals the modifications made to rules are consistent for reactions involving either species.

Sharma *et al.* [47] calculated the isomerization reactions  $\dot{R}O_2 \rightleftharpoons \dot{Q}OOH$  for a series of  $\dot{R}O_2$  radicals using the CBS-QB3 quantum chemical method as well as the isomerization and subsequent

decomposition of  $\dot{\text{O}}_2\text{QOOH}$  radicals into carbonyl-hydro peroxide species and  $\dot{\text{O}}\text{H}$  radicals. These rate constants are adopted here from analogous reactions. However, certain types of reactions which are only available for longer chain alkanes have not been calculated by Sharma *et al.* For these reactions, analogies have been made to closest representative reaction for which rate constants are available and modifications within the uncertainty range have been made. For example, the isomerization reaction  $\text{C}_6\text{H}_{13}\dot{\text{O}}_2\text{-2} \rightleftharpoons \dot{\text{C}}_6\text{H}_{12}\text{OOH2-6}$ , which occurs via an 8-membered ring transition state, has the peroxy group on a secondary carbon and involves the abstraction on a primary hydrogen atom (8sp). Unfortunately calculations for this type of reaction were not reported by Sharma *et al.* [47]. Therefore, an analogous reaction rate constant of an 8pp isomerization has been used for  $\text{C}_6\text{H}_{13}\dot{\text{O}}_2\text{-2} \rightleftharpoons \dot{\text{C}}_6\text{H}_{12}\text{OOH2-6}$ , with the A factor divided by two.

### *Thermodynamic database*

Thermodynamic data reflects the thermodynamic properties of species from which the equilibrium constants and reverse reaction rates are determined. The thermodynamic data for the *n*-hexane sub-mechanism has been determined using the software THERM [53] based on the group additivity method proposed by Benson [54]. The group values are consistent with those used for *n*-pentane [39].

## **Results and discussion**

### *Rapid Compression Machine*

Figure 5 shows the measured ignition delay time for stoichiometric *n*-hexane/air mixtures over the compressed temperature ( $T_C$ ) range of  $T_C = 627\text{--}695$  K at 15 atm (solid squares), which were measured in the RCM. The ignition delay time of stoichiometric *n*-hexane/air mixture decreases sharply with the increasing temperature. When the timescales of ignition become short compared to the compression time of the machine, the mixture may start reacting during compression, resulting in shorter ignition delay times than might be expected without reaction during compression pre-conditioning. Therefore, ignition delay times that are shorter than 5 ms may involve reaction during compression and are not presented here. Because of this limitation of the RCM and high reactivity of *n*-hexane a complementary set of ignition delay time measurements have been carried out in a high pressure shock tube over the NTC region and also at higher temperatures.

The rapid compression machine ignition delay measurements were simulated using the closed homogenous batch reactor code in CHEMKIN PRO [55]. The ignition delay time in both the rapid compression machine and the high pressure shock tube simulations is defined as the time from maximum compression or shock arrival at the endwall, respectively, to the maximum pressure rise rate due to ignition. Considering the facility effects, variable volume-time histories have been used to account for the

facility effects, which mainly include heat losses to the walls [56]. As shown in Fig. 5, the agreement between the experiments and the simulations is satisfactory except at 696 K, where the ignition delay times become very short and may be heavily influenced by reactions during the compression process.

Compared with *n*-pentane and/or *n*-butane, *n*-hexane is more reactive at low temperatures and has shorter ignition delay times at similar conditions [39, 57]. Since the uni-molecular decompositions are not significant reactions at low temperatures, the high reactivity of *n*-hexane compared to smaller alkanes is mainly due to its longer carbon chain that contains more secondary hydrogen atoms. Rather, the fuel is mainly consumed by hydrogen abstraction reactions producing fuel-derived radicals, which go through addition to O<sub>2</sub> and readily isomerizes into QOOH radicals via internal hydrogen abstraction. During this process secondary hydrogen atoms are favored in both the hydrogen abstraction reactions and in the internal hydrogen abstractions. The isomerization process favors six-membered ring transition states that consist of three carbon atoms, two oxygen atoms and one hydrogen atom due to their low ring strain. There are four secondary carbon atoms in *n*-hexane, so that each RÖ<sub>2</sub> radical produced from H-atom abstraction and further addition to O<sub>2</sub> can easily isomerize to a QOOH radical by internal H-atom abstraction from another secondary carbon atom via a six-membered ring. This is a highly efficient way to consume the fuel at low temperatures, which is only available for *n*-alkanes that contain six or more carbon atoms in the molecule. Therefore *n*-hexane has a higher reactivity at low temperature than shorter alkanes and its ignition characteristics are kinetically representative of larger normal alkanes.

#### *High pressure shock tube data*

The ignition delay times for *n*-hexane/air mixtures at equivalence ratios of 1.0 and 2.0 over the temperature range of 744–1365 K at pressures of 15 atm and 32 atm were measured in a high pressure shock tube, depicted as open symbols in Fig. 5. NTC behavior has been observed at  $\phi = 1$  and  $\phi = 2$ , over the temperature range of approximately 785–890 K at 15 atm. The measured ignition delay times are consistent with those reported by Zhukov et al. at similar conditions (*n*-hexane in air at  $\phi = 0.5$ , 15 atm).

The experimentally observed ignition delay times at  $\phi = 2$  are shorter than those at  $\phi = 1$  over most of the temperature range except at temperatures above 1250 K. This is because the fuel-rich condition has higher HÖ<sub>2</sub> concentration, leading to higher concentration of H<sub>2</sub>O<sub>2</sub> molecules that decompose into two ÖH radicals. The production of OH radicals from H<sub>2</sub>O<sub>2</sub> enhances reactivity and is the critical chain branching reaction at intermediate temperatures (~900–1250 K). However, at higher temperatures, the chain branching reaction  $\dot{H} + O_2 = \ddot{O} + \dot{O}H$  becomes increasingly more important.  $\dot{H}$  atoms can be readily produced from the beta-scission of the radicals produced by fuel decomposition. However, the reaction between fuel molecules and H atoms competes with the reaction of  $\dot{H} + O_2$  and therefore reduces the reactivity at high temperatures. Thus, at these higher temperatures, stoichiometric mixtures are fastest to

ignite while the reactivity of the system is reduced for fuel-rich mixtures. This trend can be observed in Fig. 5. In the NTC region and throughout most of the high-temperature region shown in the figure, the ignition delay times for fuel-rich conditions are in general shorter than those for the stoichiometric condition. At temperatures above 1250 K the ignition delay times at the stoichiometric condition becomes shorter than those for the fuel-rich condition. The ignition delay times are also shorter at the higher pressure of 32 atm compared to 15 atm as reaction rates increase with species concentration. At higher pressure conditions the NTC region is shifted higher in temperature due to the competition of  $\dot{H} + O_2 (+M) = \dot{H}O_2 (+M)$  with  $\dot{H} + O_2 = \ddot{O} + \dot{O}H$ . A similar trend in the pressure effects of NTC behavior has also been observed for *n*-heptane [16].

The high-pressure shock tube simulations were performed using the constant volume closed homogenous batch reactor code of CHEMKIN PRO [55]. This model is appropriate as the pressure rise before ignition (i.e.  $dp/dt = 3\%$  per ms) is slight. The comparison of predicted ignition delay times for the shock tube experiments demonstrating the effect of this pressure rise is shown in the Supplemental Material as Fig. S3. The reflected shock temperature and pressure were used as the initial conditions. The model reproduces the ignition delay times well and their trends with varying temperature and pressure in both the intermediate- and high-temperature regions, which can be observed in Fig. 5. The best agreement between the model and ignition delay measurements is observed for the stoichiometric condition at 15 atm, while the ignition delay times for  $\phi = 2$  at 15 atm and  $\phi = 1$  at 32 atm are slightly under-predicted. The predictions of the new model without modifications to the rate rules are shown in Fig. 5 with dashed lines. It is clear that these modifications have improved the overall agreement between the modeling and experimental results investigated in this study over the entire temperature range, especially in the NTC region. The dash-dotted lines represent the simulations without considering the alternative isomerization reactions. It can be seen that the adoption of these reactions has slightly increased the reactivity in the NTC region while reactivity has been decreased at low temperatures. As aforementioned, these reactions are expected to be more important for branched alkanes.

A flux analysis was carried out at  $\phi = 1.0$  and  $2.0$ ,  $T_c = 800$  K, 15 atm and 20% fuel consumption to determine the reactions that are important for *n*-hexane oxidation in the NTC region, the results are illustrated in Fig. 6. Only reactions which contribute more than 5% of the total fuel consumption are considered in the figure. The detailed contributions for the consumption of each species are shown in percent beside the arrows in different colors and fonts for  $\phi = 1.0$  (black, regular) and  $\phi = 2.0$  (red, bold and underlined).

The consumption of the fuel is shown at the top left part of Fig. 6. H-atom abstraction by  $\dot{O}H$  radicals on the secondary carbons that form  $\dot{C}_6H_{13-2}$  radicals is the most favored, while the formation of  $\dot{C}_6H_{13-1}$  radicals is least favored due to the stronger primary C–H bonds. From Fig. 5 it can be seen that

$T_C = 800$  K is near the low temperature end of the NTC region at 15 atm, thus the chain branching process of low temperature chemistry dominates the reactivity of the system. The consumption of fuel-derived radicals is mainly through chain propagating and branching sequence of first addition to  $O_2 \rightarrow$  isomerization  $\rightarrow$  second addition to  $O_2 \rightarrow$  isomerization and decomposition.

At  $\phi = 1.0$ , 90% of  $\dot{C}_6H_{13-2}$  radicals add to molecular oxygen, producing  $C_6H_{13}\dot{O}_2-2$  peroxy radicals, as shown in the lower left part of Fig. 6. In the subsequent isomerization reactions two  $\dot{Q}OOH$  radicals,  $\dot{C}_6H_{12}OOH2-4$  and  $\dot{C}_6H_{12}OOH2-5$  are mainly produced via six- and seven-membered ring transition states, respectively. As mentioned earlier, the former radical is favored (36.9% of total consumption) because of the low ring strain energy for six-membered rings. Concerted  $H\dot{O}_2$  eliminations consume 32.3% of  $C_6H_{13}\dot{O}_2-2$  radicals, reducing the reactivity by producing olefins and  $H\dot{O}_2$  radicals.  $\dot{Q}OOH$  radicals are mainly consumed by addition to  $O_2$  (2<sup>nd</sup> addition to  $O_2$ ). However, the formation of cyclic ethers and the decomposition by beta-scission are competitive with comparable contributions of 31% for  $\dot{C}_6H_{12}OOH2-4$  and over 50% for  $\dot{C}_6H_{12}OOH2-5$ , at stoichiometric conditions. These pathways are more important as the temperature increases, inhibiting the chain-branching step, thus contributing to the NTC behavior. After the second addition to  $O_2$ ,  $C_6H_{12}OOH2-4\dot{O}_2$  radicals dominantly isomerize into a ketohydroperoxide via the six-membered ring transition state. In comparison, to the  $C_6H_{12}OOH2-5\dot{O}_2$  radical, the alternative isomerization producing di-hydroperoxide radical is favored with a contribution of 62%. Moreover, the formation of the ketohydroperoxide only contributes about 27% to the total consumption of  $C_6H_{12}OOH2-5\dot{O}_2$  radical, since it proceeds through an unfavorable seven-membered ring transition state which has a higher ring strain energy than that of a six-membered ring. The decomposition of di-hydroperoxide radicals have multiple product channels; (i) the scission of a C–O bond leading to olefinic hydroperoxides when the radical site is on the beta carbon of the hydroperoxyl group, (ii) the formation of hydroperoxyl cyclic ethers and the scission of the carbon chain producing olefinic hydroperoxides plus hydroperoxide radicals. All of the products then go through further decomposition to produce smaller molecular species. Thus, in total, the first channel produces an  $H\dot{O}_2$  radical and an  $\dot{O}H$  radical which reduces the reactivity at low temperatures, while the second and the third channels both act as chain branching steps by producing two  $\dot{O}H$  radicals and an alkoxy radical thereby promoting reactivity. The contributions of these channels vary depending both on the locations of hydroperoxyl groups as well as on the radical site.

The consumption pathways for  $\dot{C}_6H_{13-3}$  radicals are slightly similar to those for the  $\dot{C}_6H_{13-2}$  radicals, however considerable amounts of  $C_6H_{13}\dot{O}_2-3$  radicals are consumed via concerted  $H\dot{O}_2$  elimination which is not a dominant pathway for the  $\dot{C}_6H_{13-2}$  radicals. The isomerization of  $C_6H_{13}\dot{O}_2-3$  radicals mainly produces  $\dot{C}_6H_{12}OOH3-5$  radicals. Meanwhile the production of  $\dot{C}_6H_{12}OOH3-1$  radicals, which are also a possible product of isomerization, is not significant. However, for  $\dot{C}_6H_{13-1}$  radicals the consumption



pathways are more complicated compared to those of  $\dot{C}_6H_{13-2}$  and  $\dot{C}_6H_{13-3}$  radicals because the hydroperoxyl group is on a primary carbon which has relatively stronger C–H bonds. Approximately 16.4% of  $\dot{C}_6H_{13-1}$  radicals isomerizes into  $\dot{C}_6H_{13-2}$  radicals, shown in the upper part of Fig. 6. Although the addition to  $O_2$  is the dominant consumption reaction, the subsequent chain propagation and branching steps are heavily influenced by the formation of olefins, cyclic ethers and olefinic hydroperoxides. For  $C_6H_{13}\dot{O}_2-1$  radical, the isomerization via 7 membered ring transition state appears more competitive than that of a 6 membered ring transition state, although the rate of the latter is higher according to the rate constants used. The simulated results indicate that this is because the  $\dot{Q}OOH$  radical that is produced in the former reaction is readily consumed to form a cyclic ether.

Through the comparison of the fates of different  $\dot{O}_2QOOH$  radicals, it appears that the alternative isomerization is generally more competitive than the formation of keto-hydroperoxides via seven-membered ring transition states but less than those via six-membered ring transition states. However, the rate rules used for the alternative isomerizations in this work are identical with those for  $\dot{Q}OOH$  isomerization, which did not take the influence of the hydroperoxyl group into consideration. Therefore the rate rules for these reactions may need to be further investigated.

In general for fuel-rich ( $\phi = 2$ ) conditions the chain branching processes are slightly inhibited compared to that at  $\phi = 1$ , which is illustrated in Fig. 6. For example, the importance of the first addition to  $O_2$ ,  $R\dot{O}_2$  isomerization, the second addition to  $O_2$  and production of keto-hydroperoxides all decrease in importance. Concurrently, the formation of olefins, cyclic ethers and the decomposition of  $R\dot{O}_2$  through beta-scissions all increase in importance. The main reason is that the temperatures of  $\phi = 2$  mixtures are higher than that of  $\phi = 1$  mixtures when 20% of fuel is consumed since the rich condition has a higher fuel concentration, although they have the same  $T_C$  at 800 K. According to the modeling predictions, the temperature the former is 861 K while that of the latter is 837 K. It is also worth noting that unlike the reactions in jet-stirred reactors, the homogenous batch reactor has varying temperatures during the ignition process, which has to be taken into consideration when comparisons are made between different mixtures at the same  $T_C$ .

A brute force sensitivity analysis was performed using CHEMKIN PRO at  $\phi = 1.0$ ,  $T_C = 800$  K and  $p_c = 15$  atm. The analyses were performed by increasing and decreasing both the forward and reverse rate constants by a factor of two. The sensitivity coefficient is expressed as follows:

$$S = \frac{\ln(\tau_+/\tau_-)}{\ln(k_+/k_-)} = \frac{\ln(\tau_+/\tau_-)}{\ln(2/0.5)}$$

A positive sensitivity coefficient indicates a reaction that inhibits the reactivity while a negative sensitivity coefficient indicates a reaction that promotes reactivity, and the results of the sensitivity analysis are shown in Fig. 7. The most sensitive reaction is the addition of  $\dot{C}_6H_{12}OOH2-4$  hydroperoxyl

alkyl radicals to  $O_2$  which promotes overall reactivity. The  $\dot{C}_6H_{12}OOH_{2-4}$  radical is produced through the most favored chain propagation pathways discussed above, and leads to chain propagation and branching via the decomposition of keto-hydroperoxides. Similarly, the addition of the  $\dot{C}_6H_{12}OOH_{3-5}$  radical to  $O_2$  is also highly sensitive. In contrast, H-atom abstraction from the fuel by  $\dot{O}H$  radicals shows different effects on fuel reactivity. The sensitivity coefficients for the formation of  $\dot{C}_6H_{13-1}$  and  $\dot{C}_6H_{13-2}$  radicals are negative, while that for the formation of the  $\dot{C}_6H_{13-3}$  radical is positive. This could be due to the relatively higher production of olefins from  $\dot{C}_6H_{13-3}$  radical as shown in the flux analysis, and the production of  $C_6$  olefins are the most important reactions inhibiting reactivity. The sensitivity analysis results also suggest that the isomerization between  $\dot{R}O_2$  and  $\dot{Q}OOH$  is faster than both the second addition to  $O_2$  and the concerted  $\dot{H}O_2$  elimination steps in the simulation, and therefore make  $\dot{R}O_2$  and  $\dot{Q}OOH$  radicals partially equilibrated. The chemistry of small molecules is not playing the most important role, while the decomposition of  $H_2O_2$  leading to chain branching and the chain terminating reaction between  $\dot{H}O_2$  radicals show considerably high sensitivity. The sensitivity analysis results at  $\phi = 2$  are similar to those at  $\phi = 1$ , with an overall decrease in sensitivity coefficients.

#### *Jet stirred reactor*

The experimental and modeling results for the oxidation of *n*-hexane in a jet-stirred reactor at 10 atm, at a residence time of 0.7 s and at equivalence ratios of 0.5, 1.0 and 2.0 are shown in Fig. 8–10 as a function of temperature. The symbols denote experimental results while the model predictions with and without the modifications in the rate rules are plotted as solid lines and dashed lines, respectively. The perfectly-stirred reactor code in CHEMIKIN PRO has been used to simulate the JSR experiments [55]. The end time of the transient calculations has been set to 20 s to allow for the system to reach steady state.

The NTC behavior of *n*-hexane is noted from the JSR data of *n*-hexane well predicted by the model at all three equivalence ratios, as shown in Fig. 8–10 (a). Good agreement between experimental and kinetic modeling results has also been observed for the major intermediates and products including CO,  $CO_2$ ,  $H_2O$ ,  $C_2H_4$ ,  $H_2$ ,  $CH_4$  and  $CH_2O$  as shown in Fig. 8–10 (b) and (c). The modifications to the reaction rate rules have increased the consumption of the reactant in the NTC region, which improves the predictions, e.g. those for CO and  $CH_2O$ . Fig. 8–10 (d) and (e) shows that the predictions for some intermediates such as  $C_3H_6$  are also good. However, the model under-predicts the concentration of  $CH_3OH$  although a slight improvement in agreement is observed with modifications in the rate rules, which indicates that rate constants for H-atom abstraction from the fuel by  $CH_3\dot{O}$  radical might need to be refined in the model. On the other hand, Dooley *et al.* [58] suggested that methanol can be produced more easily with the catalytic effect of Si-OH in an investigation of methyl butanoate oxidation in a JSR. Although *n*-hexane is not an oxygenated fuel, the oxygenated intermediates might be affected by catalysis

where this effect may contribute to deviations between the experimentally measured and modeled concentration profiles of methanol. It is worth noting that the simulated mole fraction profiles of the impurity 3-methyl pentane are also in reasonable agreement with the experimental results. Figures 8–10 (f) and (g) show some intermediates, including mainly aldehydes with long carbon chains and alkanes with high unsaturation. Most of these mole fraction profiles are well-reproduced by the model. The effects of the modifications to the reaction rate rules generally improve agreement, especially for the predictions of the aldehydes acetaldehyde, propanal and butanal, as shown in Fig. 8–10, (d)–(f).

The mole fraction profiles for important cyclic ether intermediates produced in the NTC region are presented in Fig. 8–10 (h). Three C<sub>6</sub> cyclic ethers have been measured: C<sub>6</sub>H<sub>12</sub>O<sub>2</sub>-5 (2,5-dimethyl-tetrahydrofuran, *cis* and *trans*), C<sub>6</sub>H<sub>12</sub>O<sub>2</sub>-4 (2-methyl, 4-ethyl-oxetane) and C<sub>6</sub>H<sub>12</sub>O<sub>1</sub>-4 (2-ethyl-tetrahydrofuran). C<sub>6</sub>H<sub>12</sub>O<sub>2</sub>-5 has the highest concentration among the three cyclic ethers. This is similar to the trend observed by Herbinet *et al.* [59] for the oxidation of *n*-heptane, in which the 2-ethyl, 5-methyl-tetrahydrofuran (*cis* and *trans*) showed obviously higher concentrations compared to the other C<sub>7</sub> cyclic ethers that were detected. This trend has been well captured by the model at all three equivalence ratios.

The experimentally measured concentrations and the corresponding kinetic modeling predictions for hexenes, which is another important intermediate class of product species, are shown in Fig. 8–10 (i). C<sub>6</sub> olefins can be readily produced from RO<sub>2</sub> radicals by HO<sub>2</sub> elimination reactions, which initiate an important pathway that reduces the reactivity of the system. In this work, all of the isomers of *n*-hexene have been detected. The mole fractions of the three hexene isomers are generally similar. The model over-predicts the formation of 2-hexene at around 800 K at  $\phi = 1.0$  and 2.0, but in general well predicts the mole fraction profiles for all three hexenes over the temperature range at all three equivalence ratios. It can be seen that the predictions for the cyclic ethers, especially C<sub>6</sub>H<sub>12</sub>O<sub>2</sub>-5 and C<sub>6</sub>H<sub>12</sub>O<sub>1</sub>-4, have been greatly improved by the modifications in the reaction rate rules for cyclic ether formation. Although the mole fraction of C<sub>6</sub>H<sub>12</sub>-2 is slightly over-predicted, C<sub>6</sub>H<sub>12</sub>-1 and C<sub>6</sub>H<sub>12</sub>-3 are better predicted.

Figure 11 shows a flux analysis for the oxidation of *n*-hexane in jet-stirred reactor at 950 K when the system has reached steady state. At this temperature the effect of low temperature reactions is expected to be very small. The reaction pathways shown here are dominated by high temperature reactions, opposed to the low-temperature chemistry shown in Fig. 4. The contribution of each reaction pathway has been marked with different fonts:  $\phi = 0.5$  (black, regular),  $\phi = 1.0$  (red, italic),  $\phi = 2.0$  (blue, underlined). The consumption of the fuel occurs mainly through H-atom abstractions by the radical pool, which produces the three possible fuel-derived radicals. Reactions involving the isomerization of fuel radicals become important at 950 K. These reactions are responsible for about 70% of  $\dot{C}_6H_{13}-1$  radical consumption which in turn form  $\dot{C}_6H_{13}-2$  and  $\dot{C}_6H_{13}-3$  radicals. At high temperatures the remaining fuel

derived radicals readily decompose into smaller molecules and radicals. Addition of fuel radicals to  $O_2$  becomes much less important at elevated temperatures, where only a small amount of  $RO_2$  is produced from  $\dot{C}_6H_{13-2}$  and  $\dot{C}_6H_{13-3}$  radicals, the contributions of which are below 5% at stoichiometric and fuel-rich conditions. The subsequent chain branching pathways of the small amounts of  $RO_2$  radicals that are produced are inhibited by the competition of  $HO_2$  elimination, cyclic ether formation and beta-scission reactions. The high-temperature chemistry is not significantly influenced by the modifications made to the literature rate rules, in contrast to causing substantial improvements for mechanism predictions at low-temperature conditions.

Other validations of the mechanism were made using ignition delay times, speciation in flow reactors and laminar flame speeds from literature [25-26, 60], and are included in the Supplemental Material as Fig. S4–S9. The comparisons of the current mechanism and previously reported mechanisms for *n*-hexane [17, 29] have also been included as Fig. S10–S13.

#### *Application of the reaction rate rules and modifications to n-heptane*

Since *n*-hexane is a transportation fuel relevant normal alkane, it is also interesting to see whether the reaction rate rules and these modifications could also be applied to larger normal alkanes such as *n*-heptane. A detailed kinetic model has been developed for *n*-heptane in a hierarchical manner using the *n*-hexane mechanism that was presented in this work as the basis. However, the detailed development of the *n*-heptane mechanism will not be discussed here. In brief, the reaction pathways shown in Fig. 4 were considered. All the reaction rate rules and modifications to these rules that have been utilized for *n*-hexane have also been applied to the corresponding reaction types for the *n*-heptane model. No further refinement to the rate constants has been performed to improve agreement between model predictions and experimental data. Only two representative examples will be shown here as the focus of this work is on *n*-hexane oxidation despite the numerous data sets that are available for *n*-heptane. Figure 12 shows the predictions for the *n*-heptane model simulating ignition delay times in a shock tube, compared to the experimental data reported by Ciezki *et al.* [16]. Over the wide temperature and pressure ranges shown in Fig. 12, very good agreement has been achieved between the experimental and modeling results. For speciation data, the work reported by Herbinet *et al.* on *n*-heptane oxidation in a JSR [59] is taken as a validation test case. The model has well reproduced the mole fraction profiles for most species, as shown in Fig. 13, although some deviations were observed for species such as *n*-butanal and *n*-pentanal, which indicates the need for minor refinements to the mechanism in the future.

## **Conclusions**

In this work, the ignition delay times of *n*-hexane have been measured for multiple mixtures at  $\phi = 1$  and  $\phi = 2$  over a wide temperature range at elevated pressures. The structure of *n*-hexane contains a long carbon chain and many secondary carbons, which leads to its high reactivity. The species during the oxidation of *n*-hexane have been investigated in a JSR over the temperature range 530–1160 K at three different  $\phi = 0.5, 1.0$  and  $2.0$ . Species including important low temperature intermediates have been identified with their mole fractions quantified in the JSR, providing valuable information for the development and validation of a kinetic model. The model has adopted reaction rates and rate rules which are mostly from recently reported high-level calculations. Based on the comparison of the model predictions with the experimental observations, modifications to the reaction rate rules have been made in order to obtain better agreement in the predicted reactivity and speciation validation targets simultaneously. In general the model has well reproduced the reactivity and speciation with satisfactory agreement with slight modifications to the rate rules. Further analysis of the model on the reaction flux and the sensitivity to the ignition delay times has revealed the main reaction pathways and the important reactions during the oxidation process of *n*-hexane. The reaction rate rules and modifications used in this work have also been applied in developing an *n*-heptane mechanism, the predictions of which show good agreement with the experimental results. This has provided a basis for developing mechanisms for larger normal alkanes and also for branched alkanes, which are the aims for our future work.

### **Acknowledgments**

At NUIG, the research leading to these results has received funding from the People Programme (Marie Curie Actions) of the European Union's Seventh Framework Programme FP7/2007-2013/ under REA grant agreement n° 607214. At CNRS, the research leading to these results has received funding from the European Research Council under the European Community's Seventh Framework Programme (FP7/2007-2013) / ERC grant agreement n° 291049 – 2G-CSafe.

## References

- [1] C. S. McEnally, L. D. Pfefferle, B. Atakan, and K. Kohse-Höinghaus, *Progress in Energy and Combustion Science*, 32, (2006) 247-294.
- [2] M. Mehl, W. J. Pitz, C. K. Westbrook, and H. J. Curran, *Proceedings of the Combustion Institute*, 33, (2011) 193-200.
- [3] C. K. Westbrook, W. J. Pitz, and H. J. Curran, *Journal of Physical Chemistry A*, 110, (2006) 6912-6922.
- [4] J. J. Hernández, J. Sanz-Argent, and E. Monedero-Villalba, *Fuel*, 133, (2014) 283-291.
- [5] S. M. Burke, J. M. Simmie, and H. J. Curran, *J. Phys. Chem. Ref. Data*, 44, (2015) 013101.
- [6] U. Burke, K. P. Somers, P. O. Toole, C. M. Zinner, N. Marquet, G. Bourque, E. L. Petersen, W. K. Metcalfe, Z. Serinyel, and H. J. Curran, *Combust. Flame*, 162, (2015) 315-330.
- [7] P. Dagaut, M. Cathonnet, and J. C. Boettner, *Int. J. Chem. Kinet.*, 23, (1991) 437-455.
- [8] P. Dagaut, M. Cathonnet, and J. C. Boettner, *Int. J. Chem. Kinet.*, 24, (1992) 813-837.
- [9] P. Dagaut, J. Luche, and M. Cathonnet, *Proc. Combust. Inst.*, 28, (2000) 2459-2465.
- [10] P. Dagaut, J. Luche, and M. Cathonnet, *Energy & Fuels*, 14, (2000) 712-719.
- [11] A. J. Eskola, O. Welz, J. Zádor, I. O. Antonov, L. Sheps, J. D. Savee, D. L. Osborn, and C. A. Taatjes, *Proc. Combust. Inst.*, 35, (2015) 291-298.
- [12] O. Herbinet, F. Battin-Leclerc, S. Bax, H. L. Gall, P. A. Glaude, R. Fournet, Z. Zhou, L. Deng, H. Guo, M. Xie, and F. Qi, *Physical Chemistry Chemical Physics*, 13, (2011) 296-308.
- [13] W. K. Metcalfe, S. M. Burke, S. S. Ahmed, and H. J. Curran, *Int. J. Chem. Kinet.*, 45, (2013) 638-675.
- [14] C. J. Aul, W. K. Metcalfe, S. M. Burke, H. J. Curran, and E. L. Petersen, *Combust. Flame*, 160, (2013) 1153-1167.
- [15] S. Ravi, T. G. Sikes, A. Morones, C. L. Keesee, and E. L. Petersen, *Proc. Combust. Inst.*, 35, (2015) 679-686.
- [16] H. Ciezki and G. Adomeit, *Combust. Flame*, 93, (1993) 421-433.
- [17] H. Curran, P. Gaffuri, W. J. Pitz, and C. K. Westbrook, *Combust. Flame*, 114, (1998) 149-177.

- [18] P. Dagaut, M. Reuillon, and M. Cathonnet, *Combust. Flame*, 101, (1995) 132-140.
- [19] J. Herzler, L. Jerig, and P. Roth, *Proc. Combust. Inst.*, 30, (2005)
- [20] E. Ranzi, P. Gaffuri, T. Faravelli, and P. Dagaut, *Combust. Flame*, 103, (1995) 91-106.
- [21] E. J. Silke, H. J. Curran, and J. M. Simmie, *Proc. Combust. Inst.*, 30, (2005) 2639-2647.
- [22] J. M. Smith, J. M. Simmie, and H. J. Curran, *Int. J. Chem. Kinet.*, 37, (2005) 728-736.
- [23] A. Burcat, E. Olchanski, and C. Sokolinski., *Isr. J. Chem.*, 36, (1996) 313-320.
- [24] H. J. Curran, P. Gaffuri, W. J. Pitz, C. K. Westbrook, and W. R. Leppard, *Proc. Combust. Inst.*, 26, (1996) 2667-2677.
- [25] R. Mével, K. Chatelain, P. A. Boettcher, and J. E. Shepherd, 8th US National Combustion Meeting, University of Utah, May 19-22, 2013, 070RK-0399.
- [26] V.P. Zhukov, V. A. Sechenov, and A. Y. Starikovskii, *Combust. Flame*, 136, (2004) 257-259.
- [27] Z. Wang, O. Herbinet, Z. Cheng, B. Husson, R. Fournet, F. Qi, and F. Battin-Leclerc, *J. Phys. Chem. A*, 118, (2014) 5573-5594.
- [28] H. J. Curran, P. Gaffuri, W. J. Pitz, C. K. Westbrook, and W. R. Leppard, SAE Technical Paper 952406, 1995, doi:10.4271/952406.
- [29] H. P. Ramirez, K. Hadj-Ali, P. Dievart, G. Dayma, C. Togbe, G. Moreac, and P. Dagaut., *Proc. Combust. Inst.*, 33, (2011) 375-382.
- [30] F. Qi, *Proc. Combust. Inst.*, 34, (2013) 33-63.
- [31] F. Battin-Leclerc, *Progress in Energy and Combustion Science*, 34, (2008) 440-498.
- [32] W. S. Affleck and A. Thomas, *Proc. Inst. Mech. Eng.*, 183, 365-385.
- [33] L. Brett, J. Macnamara, P. Musch, and J. M. Simmie, *Combust. Flame*, 124, (2001) 326-329.
- [34] D. Darcy, H. Nakamura, C. J. Tobin, M. Mehl, W. K. Metcalfe, W. J. Pitz, C. K. Westbrook, and H. J. Curran, *Combust. Flame*, 161, (2014) 65-74.
- [35] J. Würmel and J. M. Simmie, *Combust. Flame*, 141, (2005) 417-430.
- [36] H. Nakamura, D. Darcy, M. Mehl, C. J. Tobin, W. K. Metcalfe, W. J. Pitz, C. K. Westbrook, and H. J. Curran, *Combust. Flame*, 161, (2014) 49-64.
- [37] P. Dagaut, M. Cathonnet, J. Rouan, R. Foulatier, A. Quilgars, J. Boettner, F. Gaillard, and H. James, *Journal of Physics E: Scientific Instruments*, 19, (1986) 207-209.

- [38] P. Dagaut, F. Karsenty, G. Dayma, P. Diévert, K. Hadj-Ali, A. Mzé-Ahmed, T. Kick, J. Herbst, T. Kathrotia, M. Braun-Unkhoff, J. Herzler, C. Naumann, and U. Riedel, *Combust. Flame*, 161, (2014) 835-847.
- [39] J. Bugler, K. P. Somers, E. J. Silke, and H. J. Curran, *J. Phys. Chem. A*, An investigation of the thermochemical parameter and rate coefficient assignments for the low-temperature oxidation pathways of alkanes: a case study using the pentane isomers, (2015) in press.
- [40] H. J. Curran, P. Gaffuri, W. Pitz, and C. Westbrook, *Combust. Flame*, 129, (2002) 253-280.
- [41] S. Rolland and J. M. Simmie, *Int. J. Chem. Kinet.*, 37, (2005) 119-125.
- [42] M. Pelucchi, K. P. Somers, K. Yasunaga, U. Burke, A. Frassoldati, E. Ranzi, H. J. Curran, and T. Faravelli, *Combustion and Flame*, 162, (2015) 265-286.
- [43] A. W. Jasper and J. A. Miller, *Combust. Flame*, 161, (2014) 101-110.
- [44] R. Sivaramakrishnan and J. V. Michael, *J. Phys. Chem. A*, 113, (2009) 5047-5060.
- [45] W. Tsang, J. A. Walker, and J. A. Manion, *Proc. Combust. Inst.*, 31, (2007) 141-148.
- [46] C. F. Goldsmith, W. H. Green, and S. J. Klippenstein, *J. Phys. Chem. A*, 116, (2012) 3325-3346.
- [47] S. Sharma, S. Raman, and W. H. Green, *J. Phys. Chem. A*, 114, (2010) 5689-5701.
- [48] S. M. Villano, L. K. Huynh, H.-H. Carstensen, and A. M. Dean, *J. Phys. Chem. A*, 115, (2011) 13425-13442.
- [49] S. M. Villano, L. K. Huynh, H.-H. Carstensen, and A. M. Dean, *J. Phys. Chem. A*, 116, (2012) 5068-5089.
- [50] S. M. Villano, H.-H. Carstensen, and A. M. Dean, *J. Phys. Chem. A*, 117, (2013) 6458-6473.
- [51] A. Miyoshi, *Int. J. Chem. Kinet.*, 44, (2012) 59-74.
- [52] M. Pelucchi, M. Bissoli, C. Cavallotti, A. Cuoci, T. Faravelli, A. Frassoldati, E. Ranzi, and A. Stagni, *Energy & Fuels*, 28, (2014) 7178-7193.
- [53] E. R. Ritter and J. W. Bozzelli, *Int. J. Chem. Kinet.*, 23, (1991) 767-778.
- [54] S. W. Benson, *Thermochemical Kinetics*, 2nd ed., Wiley: New York, 1976.
- [55] J. Andersen, P. A. Jensen, S. L. Hvid, and P. Glarborg, *Energy & Fuels*, 23, (2009) 5783-5791.



- [56] C.-J. Sung and H. J. Curran, *Progress in Energy and Combustion Science*, 44, (2014) 1-18.
- [57] D. Healy, N. S. Donato, C. J. Aul, E. L. Petersen, C. M. Zinner, G. Bourque, and H. J. Curran, *Combustion and Flame*, 157, (2010) 1526-1539.
- [58] S. Dooley, H. J. Curran, and J. M. Simmie, *Combust. Flame*, 153, (2008) 2-32.
- [59] O. Herbinet, B. Husson, Z. Serinyel, M. Cord, V. Warth, R. Fournet, P.-A. Glaude, B. Sirjean, F. Battin-Leclerc, Z. Wang, M. Xie, Z. Cheng, and F. Qi, *Combustion and Flame*, 159, (2012) 3455-3471.
- [60] S. Coronel, R. Mével, P. Vervish, P. A. Boettcher, V. Thomas, N. Chaumeix, N. Darabiha, and J. E. Shepherd, 8th US National Combustion Meeting, University of Utah, May 19-22, 2013, 070LT-0383.

Table 1. The detailed composition of the inlet gas mixtures in JSR experiment.

$\phi$	Inlet concentration (%)			
	n-hexane	3-methyl pentane	O <sub>2</sub>	N <sub>2</sub>
0.5	0.095	0.005	0.019	0.980
1.0	0.095	0.005	0.010	0.990
2.0	0.095	0.005	0.005	0.994

Table 2. Nomination of representative species in n-hexane sub mechanism.

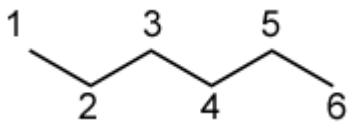
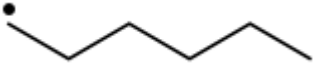

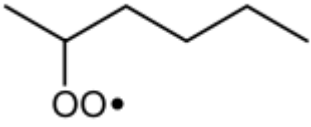
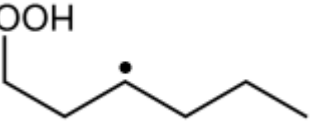
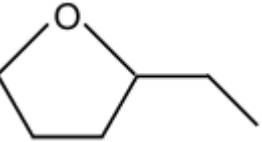
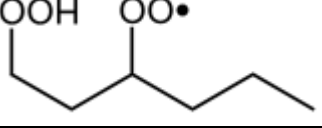
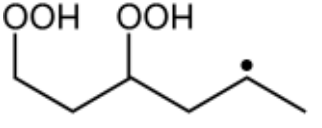
$nC_6H_{14}$	
$\dot{C}_6H_{13-1}$	
$C_6H_{12-1}$	
$C_6H_{13}\dot{O}_2-2$	
$\dot{C}_6H_{12}OOH1-3$	
$C_6H_{12}O1-4$	
$C_6H_{12}OOH1-3\dot{O}_2$	
$\dot{C}_6H_{11}Q13-5$	

Table 3. Modifications to the reaction rate rules.

Reaction	Rate rules	Details	Example
$\dot{R}O_2 \rightleftharpoons \dot{Q}OOH$	Table 6 in [47]	A $\times$ 0.5 for those using nearest analogy, which were not calculated:	
		5 member ring, O <sub>2</sub> on secondary, abstraction on primary	$C_6H_{13}\dot{O}_2-2 \rightleftharpoons \dot{C}_6H_{12}OOH2-1$
		7 member ring, O <sub>2</sub> on secondary, abstraction on secondary	$C_6H_{13}\dot{O}_2-2 \rightleftharpoons \dot{C}_6H_{12}OOH2-5$
		8 member ring, O <sub>2</sub> on secondary, abstraction on primary	$C_6H_{13}\dot{O}_2-2 \rightleftharpoons \dot{C}_6H_{12}OOH2-6$
Cyclic ether formation	Table 3 in [49]	All A factors $\times$ 0.5	
		Ea+1 kcal for:	
		CY/C4O, OOH on primary, radical on secondary	$\dot{C}_6H_{12}OOH1-4 \rightleftharpoons C_6H_{12}O1-4+\dot{O}H$
		CY/C3O, OOH on secondary, radical on secondary	$\dot{C}_6H_{12}OOH2-4 \rightleftharpoons C_6H_{12}O2-4+\dot{O}H$
		Ea-1 kcal for:	
		CY/C4O, OOH on secondary, radical on secondary	$\dot{C}_6H_{12}OOH2-5 \rightleftharpoons C_6H_{12}O2-5+\dot{O}H$
Concerted $\dot{H}O_2$ elimination	Table 4 of [48]	A $\times$ 1.5 for:	
		O <sub>2</sub> on primary, H on secondary	$C_6H_{13}\dot{O}_2-1 \rightleftharpoons C_6H_{12}-1 + \dot{H}O_2$
		O <sub>2</sub> on secondary, H on primary	$C_6H_{13}\dot{O}_2-2 \rightleftharpoons C_6H_{12}-1 + \dot{H}O_2$
		O <sub>2</sub> on S11, H on S11. (P1-S10-S11-S11-S10-P1)	$C_6H_{13}\dot{O}_2-3 \rightleftharpoons C_6H_{12}-3 + \dot{H}O_2$
Second addition to O <sub>2</sub>	Table IV of [46, 51]	A $\times$ 0.5 from the first addition to O <sub>2</sub>	$\dot{C}_6H_{12}OOH1-2+O_2 \rightleftharpoons C_6H_{12}OOH1-2\dot{O}_2$

Figure 1. An example RCM pressure trace.

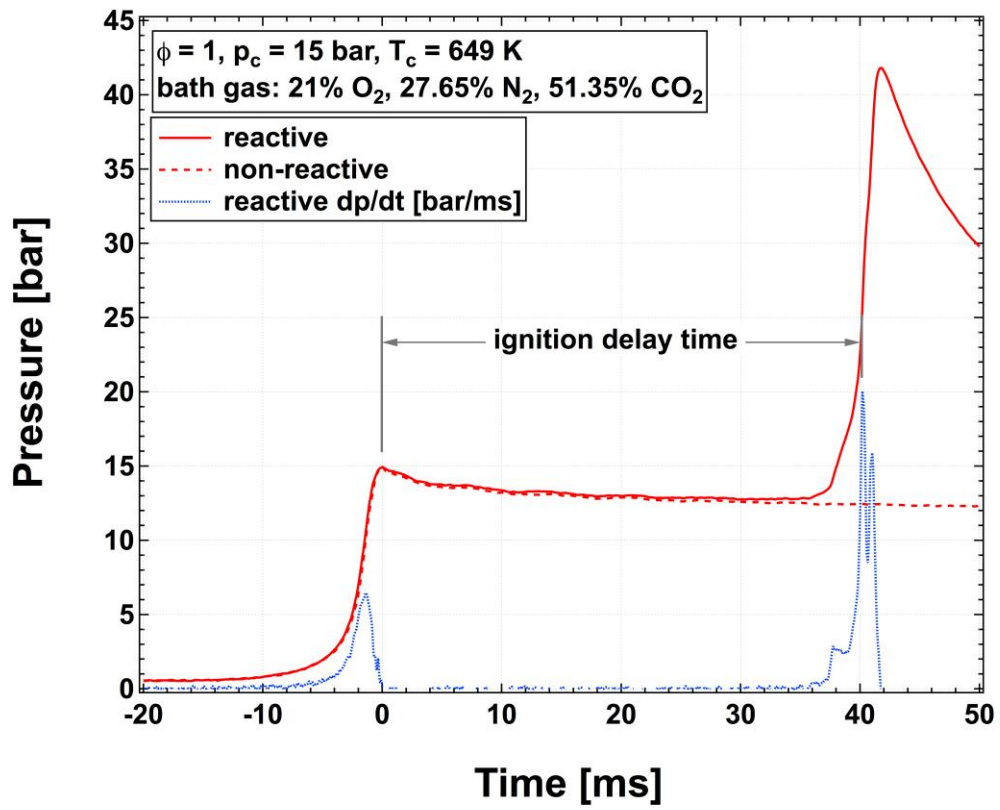


Figure 2. Schematic of the RCM piston head geometry.

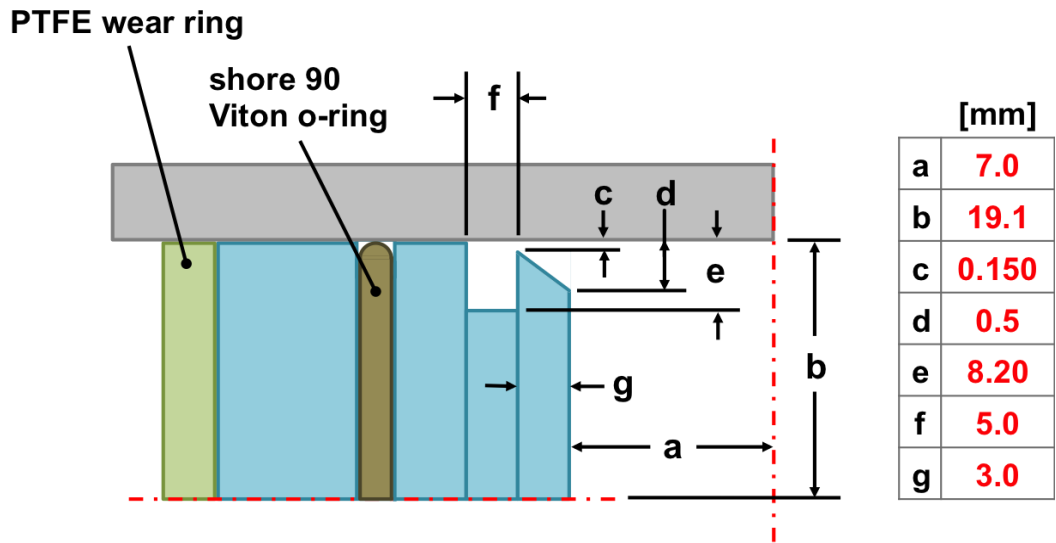


Figure 3. An example HPST endwall pressure trace

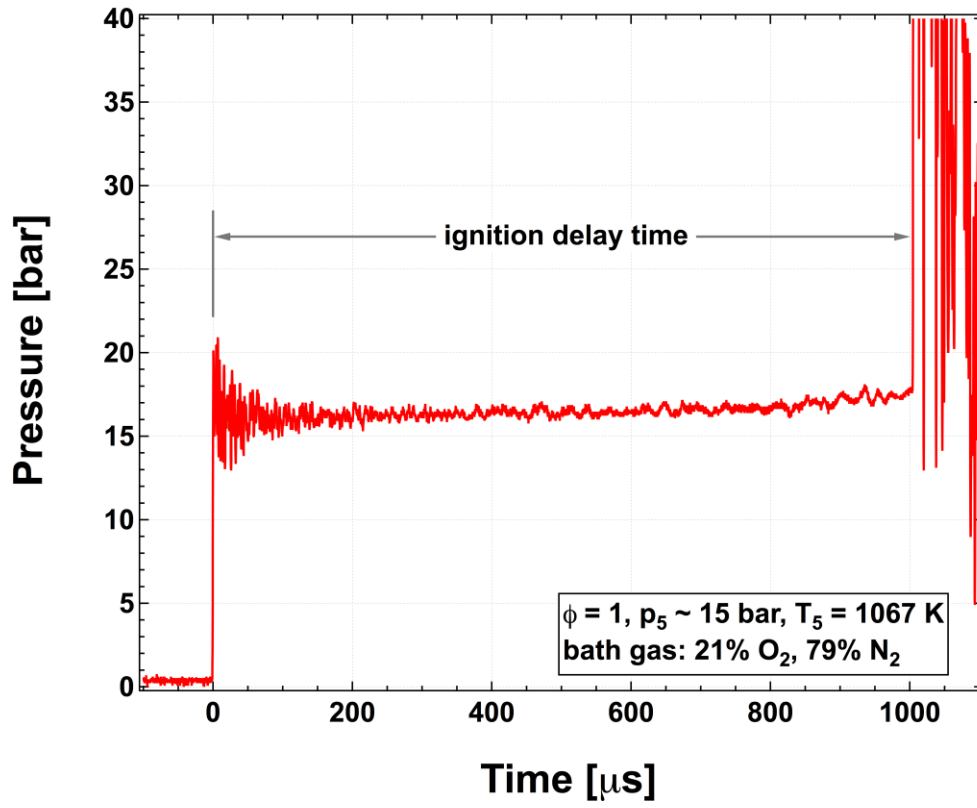
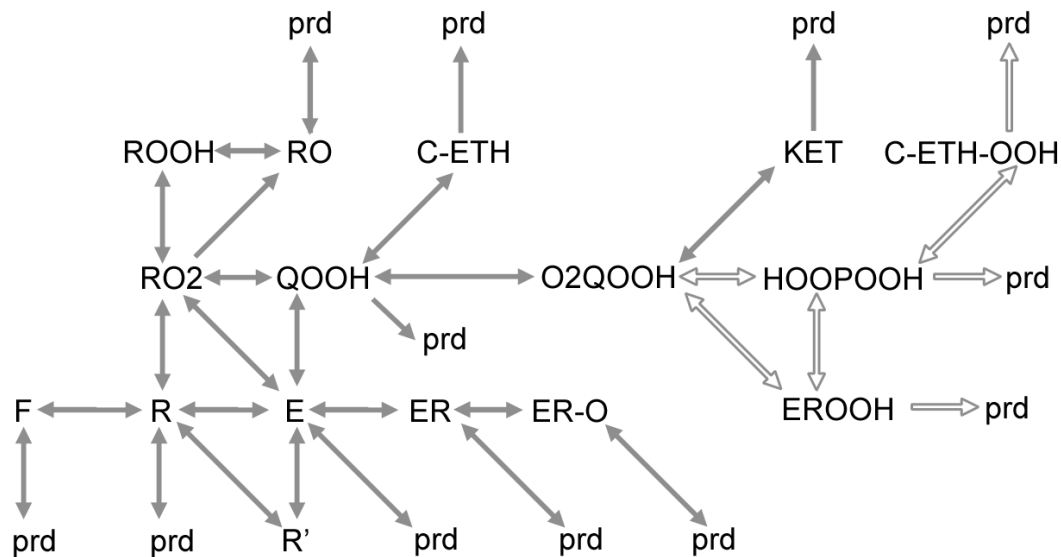


Figure 4. Reaction pathways considered in the model development of this work. The reaction pathways induced by the alternative isomerization of peroxy hydroperoxyalkyl have been marked with open arrows.



F = fuel, R = fuel derived radical, RO2 = peroxyalkyl, QOOH = hydroperoxyalkyl, ROOH = hydroperoxide  
 RO = alkoxyl, C-ETH = cyclic ether, O2QOOH = peroxy-hydroperoxyalkyl, HOOPOOH = dihydroperoxyalkyl  
 KET = keto-hydroperoxide, C-ETH-OOH = hydroperoxy cyclic ethers, EROOH = olefinic hydroperoxyalkyl  
 E = olefin, ER = olefinic radical, ER-O = olefinic alkoxy, prd = decomposition products



Figure 5. Experimental (symbols) and modeling results (lines) for *n*-hexane ignition delay times at multiple conditions. Solid symbols denote data from experiments with rapid compression machine while open symbols are those from high pressure shock tube experiments. Solid and dashed lines are predictions with and without the modifications in the rate rules, respectively. Dash-dotted lines are predictions without considering the alternative isomerization reactions.

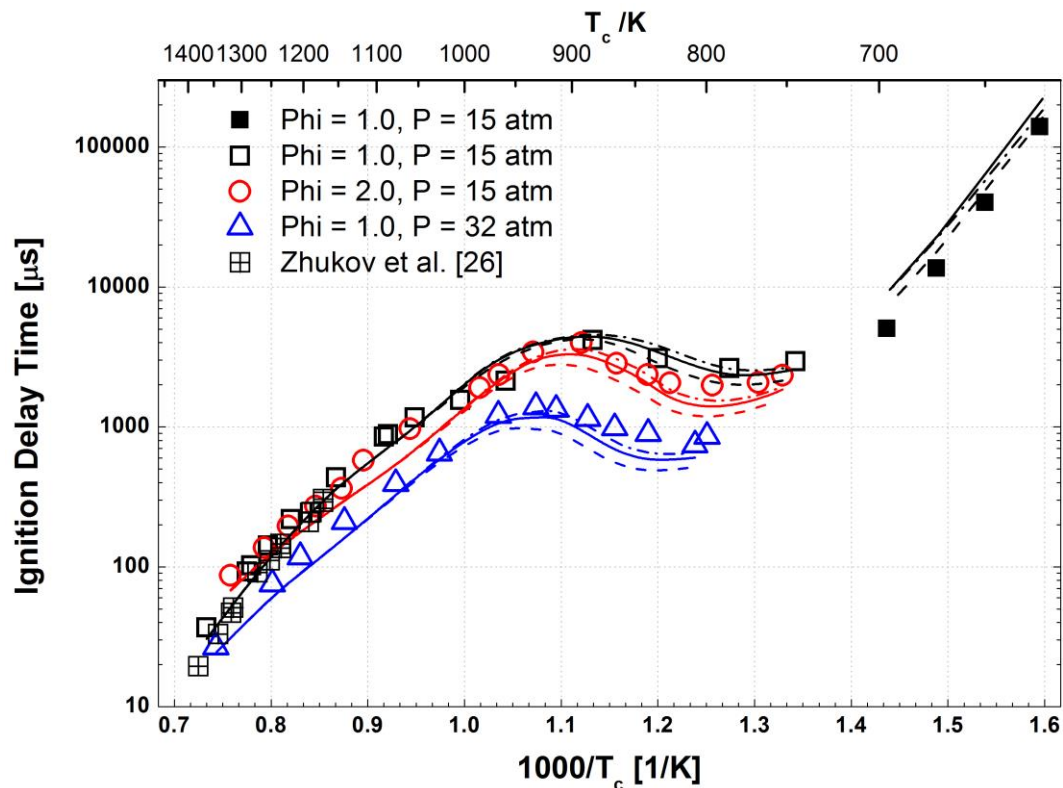


Figure 6. Reaction flux for n-hexane ignition at  $T_c = 800$  K,  $P_c = 10$  atm and 20% fuel conversion. The contributions of the reactions are marked beside the arrows. Regular and underlined numbers are for  $\phi = 1.0$  and  $\phi = 2.0$ , respectively.

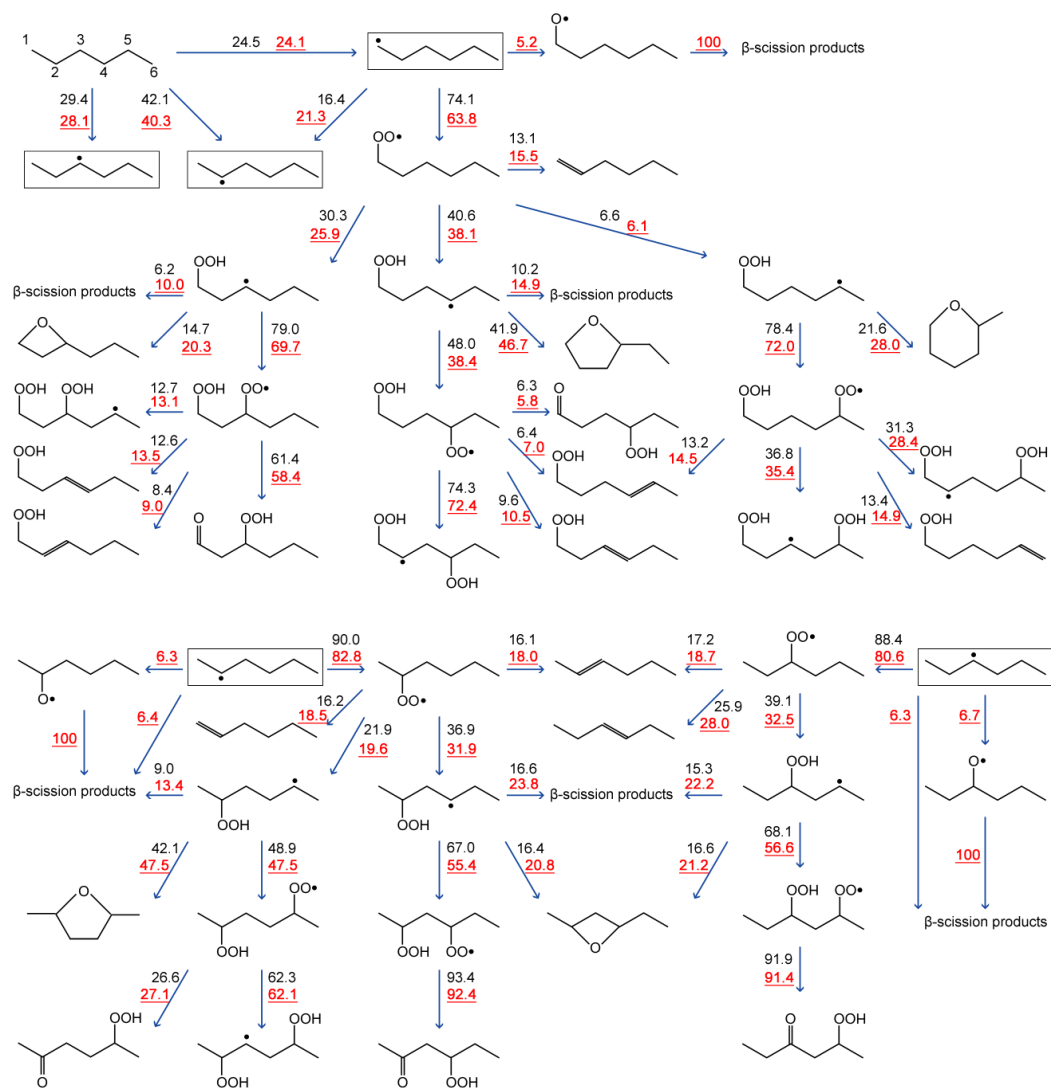


Figure 7. Sensitivity analysis on the ignition delay time of *n*-hexane at  $T_c = 800$  K and  $P_c = 15$  atm. Negative sensitivity coefficients indicate decreases in ignition delay times.

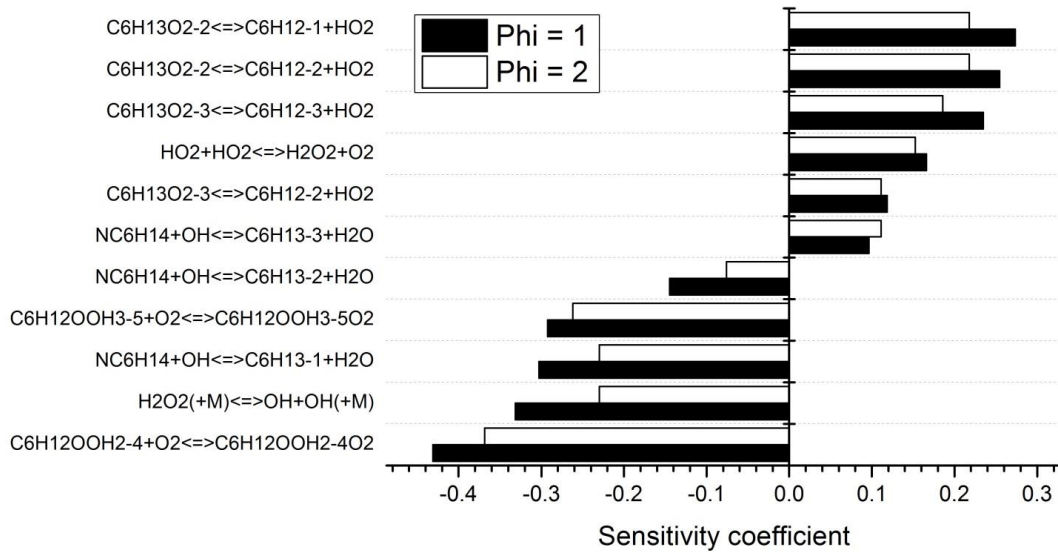


Figure 8. Experimental (symbols) and modeling results for *n*-hexane oxidation in a jet-stirred reactor at 10 atm for  $\phi = 0.5$ . Solid and dashed lines are predictions with and without the modifications in the rate rules, respectively. Dash-dotted lines are predictions without considering the alternative isomerization reactions.

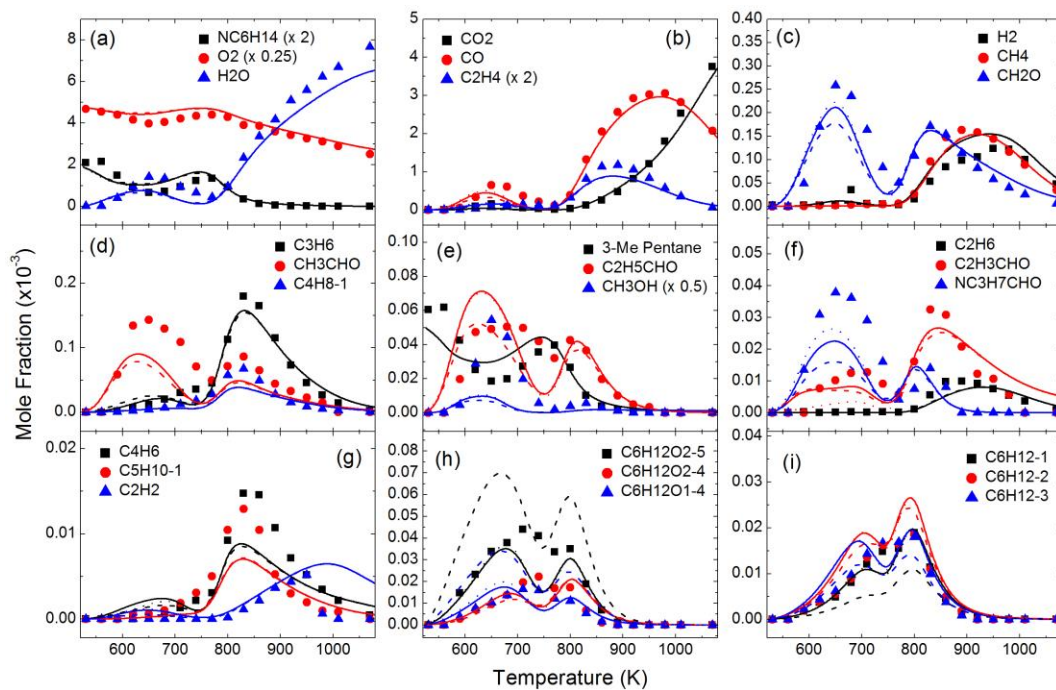


Figure 9. Experimental (symbols) and modeling results for *n*-hexane oxidation in a jet-stirred reactor at 10 atm for  $\phi = 1.0$ . Solid and dashed lines are predictions with and without the modifications in the rate rules, respectively. Dash-dotted lines are predictions without considering the alternative isomerization reactions.

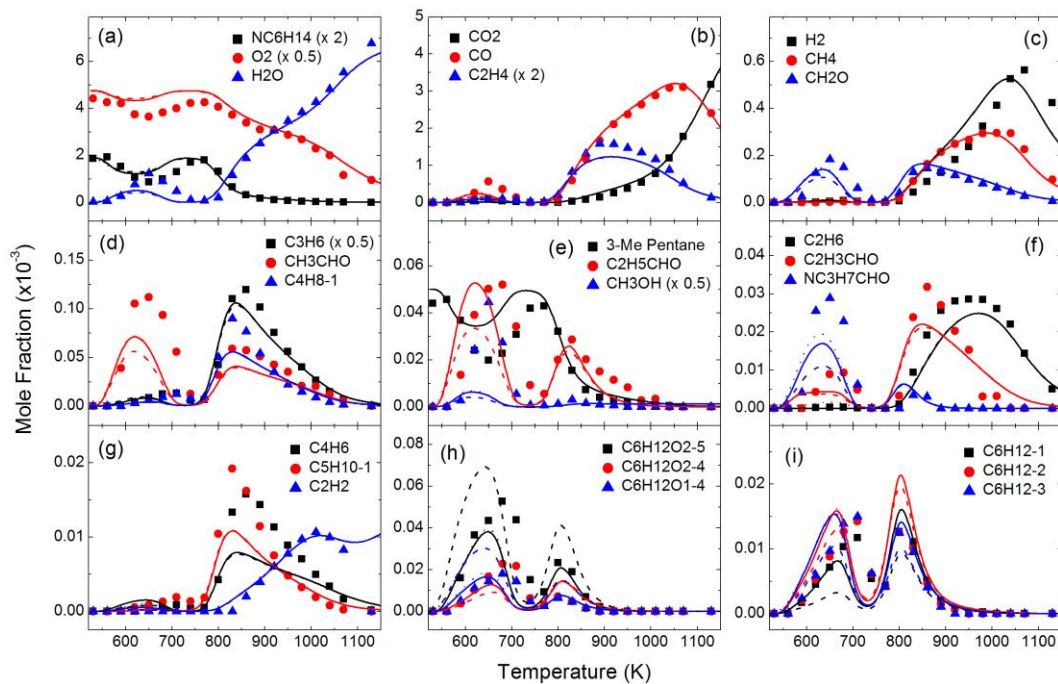


Figure 10. Experimental (symbols) and modeling results for *n*-hexane oxidation in a jet-stirred reactor at 10 atm for  $\phi = 2.0$ . Solid and dashed lines are predictions with and without the modifications in the rate rules, respectively. Dash-dotted lines are predictions without considering the alternative isomerization reactions.

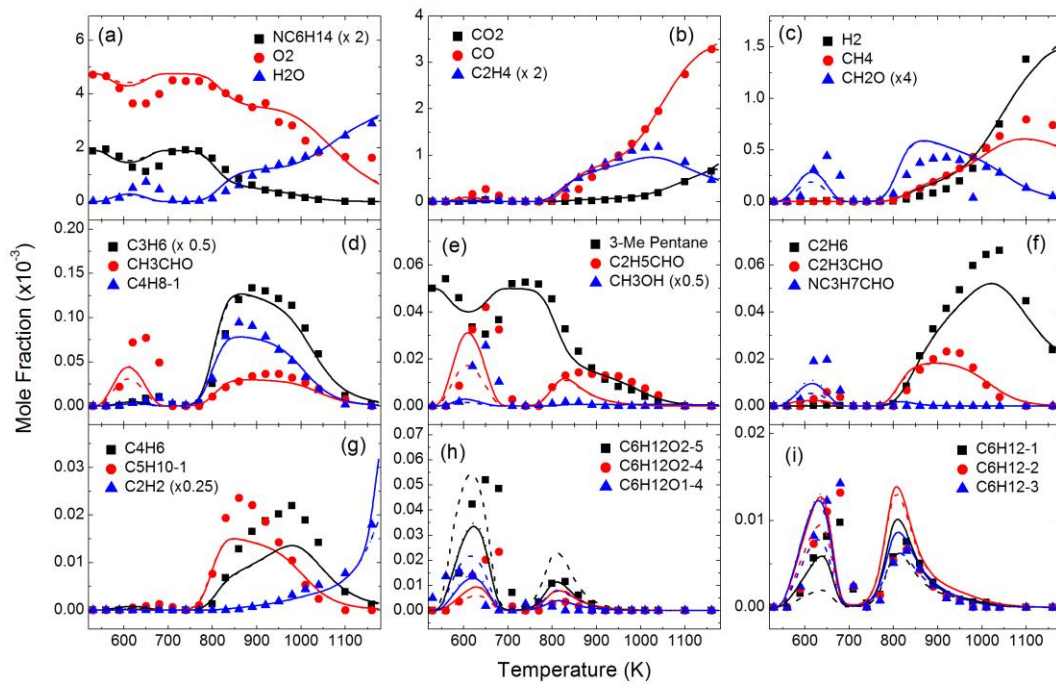


Figure 11. Reaction flux for *n*-hexane ignition at  $T_c = 950$  K,  $P_c = 10$  atm and 20% fuel conversion. The contributions of the reactions are marked beside the arrows. Regular, italic and underlined numbers are for  $\phi = 0.5$ ,  $\phi = 1.0$  and  $\phi = 2.0$ , respectively.

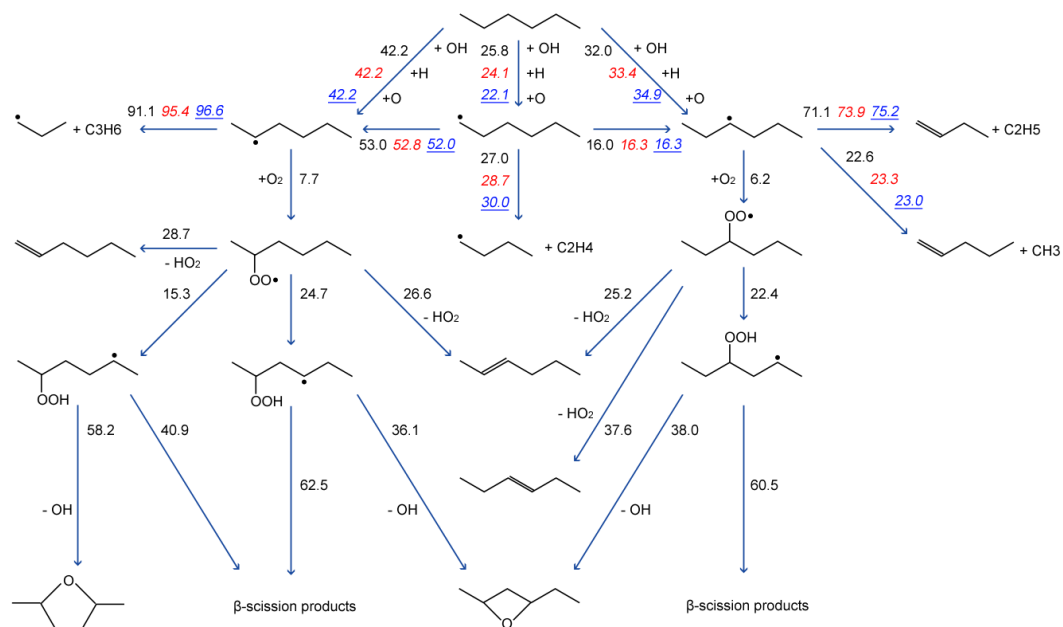


Figure 12. Experimental [16] and modeling results of ignition delay times of *n*-heptane / air mixtures in shock tube.

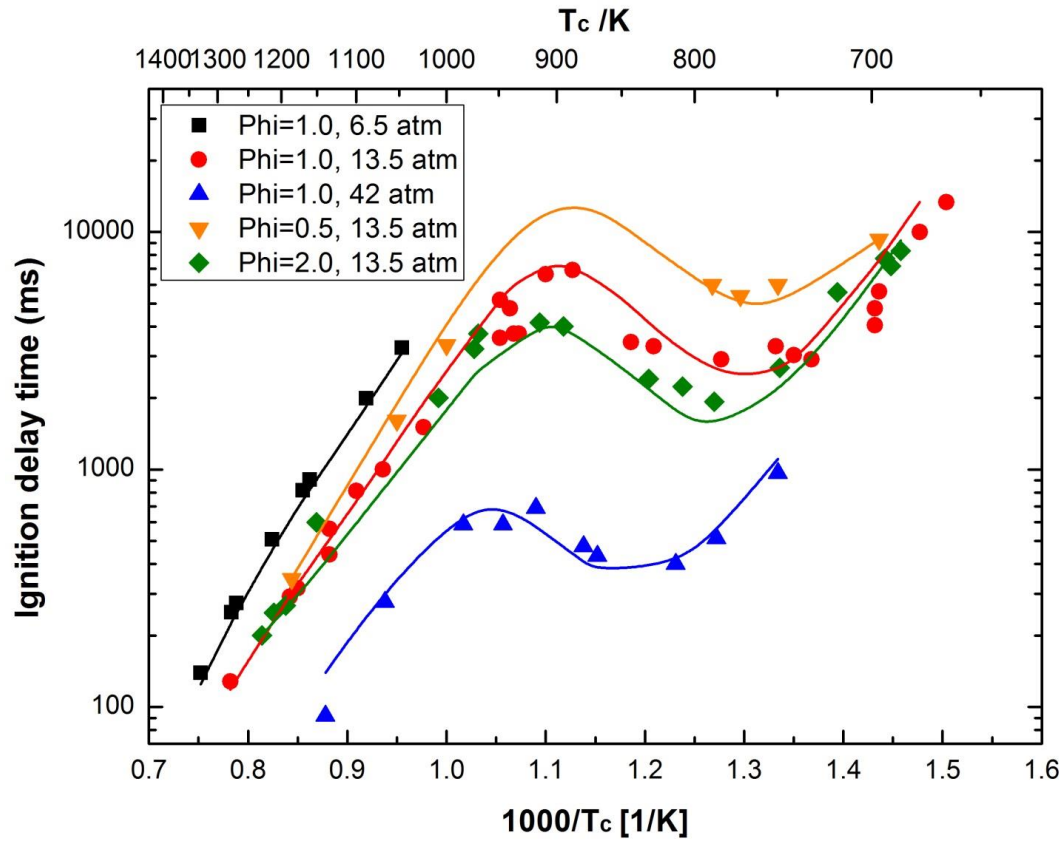




Figure 13. Experimental [59] and modeling results of *n*-heptane oxidation in a jet-stirred reactor at  $\phi = 1.0$ , 1.06 bar with the residence time at 2 s and the dilution ratio at 94% (Diluent: Helium).

